

Cellular and network mechanisms may generate sparse coding of sequential object encounters in hippocampal-like circuits

<https://doi.org/10.1523/ENEURO.0108-19.2019>

Cite as: eNeuro 2019; 10.1523/ENEURO.0108-19.2019

Received: 19 March 2019

Revised: 11 June 2019

Accepted: 12 July 2019

This Early Release article has been peer-reviewed and accepted, but has not been through the composition and copyediting processes. The final version may differ slightly in style or formatting and will contain links to any extended data.

Alerts: Sign up at www.eneuro.org/alerts to receive customized email alerts when the fully formatted version of this article is published.

Copyright © 2019 Trinh et al.

This is an open-access article distributed under the terms of the Creative Commons Attribution 4.0 International license, which permits unrestricted use, distribution and reproduction in any medium provided that the original work is properly attributed.

Title: Cellular and network mechanisms may generate sparse coding of sequential object encounters in hippocampal-like circuits

Authors: Anh-Tuan Trinh^{1*}, Stephen E. Clarke³, Erik Harvey-Girard¹, Leonard Maler^{1,2}

1. Department of Cellular and Molecular Medicine, University of Ottawa, Ottawa, Ontario, Canada

2. Brain and Mind Institute, Center for Neural Dynamics, University of Ottawa, Ottawa, Ontario, Canada

3. Department of Bioengineering, Stanford University, Stanford, CA, United States of America

Author Contributions: A.T., S.E.C., E.H-G and L.M. Designed research. A.T. and E.H-G. Performed research. A.T., S.E.C., E.H-G and L.M. Analyzed data; A.T., S.E.C and L.M. Wrote the paper.

Correspondence should be addressed to Anh-Tuan Trinh, Department of Cellular and Molecular Medicine, University of Ottawa, 451 Smyth Rd, Ottawa, ON K1H 8M5, Canada. E-mail: atrin054@uottawa.ca

9 Figures, 3 Tables, 2 Extended Figures, 1 Zip file containing Matlab code

Word numbers:

Abstract: 196 words

Significance Statement: 110 words

Introduction: 750 words

Discussion: 2411 words

Acknowledgements: We would like to thank William Ellis for technical support and Maria Lambadaris for her help with the electrophysiological recordings. We also thank Jean-Claude Béïque, Richard Naud and Timal Kannangara for their helpful discussions and suggestions.

Conflict of Interest: The authors declare no conflicting financial or non-financial interests.

Funding Source: This research was supported by the Canadian Institutes of Health Research - CIHR 153143 and by the Natural Sciences and Engineering Research Council - NSERC 04336 grant, both assigned to LM.

35 **Cellular and network mechanisms may generate sparse coding of**
36 **sequential object encounters in hippocampal-like circuits**

37

38 **Abstract**

39

40 The localization of distinct landmarks plays a crucial role in encoding new spatial
41 memories. In mammals, this function is performed by hippocampal neurons that sparsely encode
42 an animal's location relative to surrounding objects. Similarly, the dorsal lateral pallium (DL) is
43 essential for spatial learning in teleost fish. The DL of weakly electric gymnotiform fish receives
44 both electrosensory and visual input from the preglomerular nucleus (PG), which has been
45 hypothesized to encode the temporal sequence of electrosensory or visual landmark/food
46 encounters. Here, we show that DL neurons in the *Apteronotid* fish and in the *Carassius auratus*
47 (goldfish) have a hyperpolarized resting membrane potential combined with a high and dynamic
48 spike threshold that increases following each spike. Current-evoked spikes in DL cells are
49 followed by a strong small-conductance calcium-activated potassium channel (SK) mediated after-
50 hyperpolarizing potential (AHP). Together, these properties prevent high frequency and
51 continuous spiking. The resulting sparseness of discharge and dynamic threshold suggest that DL
52 neurons meet theoretical requirements for generating spatial memory engrams by decoding the
53 landmark/food encounter sequences encoded by PG neurons. Thus, DL neurons in teleost fish may
54 provide a promising, simple system to study the core cell and network mechanisms underlying
55 spatial memory.

56

57 **Significance Statement**

58

59 To our knowledge, this is first study of the intrinsic physiology of teleost pallial (DL)
60 neurons. Their biophysical properties demonstrate that DL neurons are sparse coders with a
61 dynamic spike threshold leading us to suggest that they can transform time-stamped input into
62 spatial location during navigation. The concept of local attractors (bumps) that potentially move
63 ‘across’ local recurrent networks has been prominent in the neuroscience theory literature. We
64 propose that the relatively simple and experimentally accessible DL of teleosts may be the best
65 preparation to examine this idea experimentally and to investigate the properties of local
66 (excitatory) recurrent networks whose cells are endowed with, e.g., slow spike threshold
67 adaptation dynamics.

68 Introduction

69

70 The mammalian hippocampus is required for the storage and recall of spatial memory that
71 presumably guides path integration and landmark based navigation (Barry and Burgess, 2014;
72 Hartley et al., 2014). Conventionally, sparse discharge of dentate gyrus (DG) granule cells and
73 CA1/CA3 pyramidal cells can encode a rodent's location with respect to visually identified
74 landmarks (Barry and Burgess, 2014; Hartley et al., 2014). An emerging alternate view of
75 hippocampal function emphasizes its role in the encoding of temporal sequences within or across
76 periods of locomotion (Pastalkova et al., 2008; MacDonald et al., 2011; Kraus et al., 2013;
77 Eichenbaum, 2014; Modi et al., 2014; Ranganath and Hsieh, 2016). For example, hippocampal
78 neurons may discharge at specific times after the initiation of running and effectively tile an entire
79 running episode (Kraus et al., 2013). The encoding of time and location appears to be closely
80 connected with the responses of a subset of neurons to time spent and distance travelled (Kraus et
81 al., 2013; Deuker et al., 2016; Eichenbaum, 2017).

82

83 Visuospatial memory is also important for teleost fish (Rodriguez et al., 2002) and they
84 can learn to finely discriminate between visual inputs (Schluessel and Bleckmann, 2005; Siebeck
85 et al., 2009; Rischawy and Schuster, 2013; Newport et al., 2016). Unlike mammals, fish do not
86 have an obvious cortex or hippocampus; instead, their dorsal telencephalon (pallium) is divided
87 into non-layered cell groups that have specific connectivity and function (Rodríguez et al., 2002;
88 Northcutt, 2008; Giassi et al., 2012b; Giassi et al., 2012c). Visual input to the pallium primarily
89 arrives from the optic tectum and reaches the dorsolateral pallium (DL) through the thalamus-like
90 preglomerular nucleus (PG, Yamamoto and Ito, 2008; Giassi et al., 2012b; Wallach et al., 2018).

91 Lesion studies have shown that DL is essential for visual (landmark) based spatial learning and
 92 memory (Rodriguez et al., 2002).

93

94 Comparisons of teleost pallium to mammalian dorsal telencephalon has been controversial,
 95 and similarity between DL and either hippocampus or cortex have been stressed. Based on its
 96 location (Yamamoto et al., 2007; Mueller and Wullimann, 2009), extrinsic connections (Elliott et
 97 al., 2017) and molecular markers (Harvey-Girard et al., 2012; Ganz et al., 2014), it has been
 98 proposed that DL is homologous to the hippocampus (in particular to DG, Elliott et al., 2017).
 99 However, unlike the major recipients of sensory information in the hippocampal formation (*i.e.*,
 100 DG, CA1), DL neurons have strong local recurrent connectivity (Trinh et al., 2016). DL's extrinsic
 101 and intrinsic connectivity also suggests a strong resemblance to the mammalian cortex (Yamamoto
 102 et al., 2007; Giassi et al., 2012b; Trinh et al., 2016; Elliott et al., 2017). However, DL neurons are
 103 morphologically very different from both DG granule cells and the pyramidal cells of the
 104 hippocampus and cortex (Giassi et al., 2012c).

105

106 A teleost subgroup, the weakly electric gymnotiform fish, can use their electrosensory
 107 system to finely discriminate temporal (Harvey-Girard et al., 2010) and spatial (Graff et al., 2004;
 108 Dangelmayer et al., 2016) patterns and use electrosensory-identified landmarks to learn the spatial
 109 location of food (Jun et al., 2016). Electrosensory input is first processed in the hindbrain
 110 electrosensory lobe (ELL) and, via a midbrain relay, then mapped onto the tectum (Krahe and
 111 Maler, 2014). Electrosensory and visual tectal cells then project to PG and their PG target then
 112 projects exclusively to DL (Giassi et al., 2012b). Two recent studies have shown that DL cells can
 113 process visual and electrosensory inputs. In goldfish, Vinepinsky et al. (2018) have described DL

114 cells responsive to boundaries (visual input) as well as speed and direction of self-motion. In a
115 gymnotiform fish, neurons within a major target of DL (dorsal pallium, DD) have been shown to
116 discharge to the electrosensory signals generated when the fish moves near ‘landmarks’ (Fotowat
117 et al., 2019).

118

119 Recently, a subset of electrosensory motion PG neurons have been identified that can
120 encode the time interval between object encounters (Wallach et al., 2018). Wallach et al.
121 hypothesize that the output of these ‘time stamp’ neurons is used to estimate the distance between
122 the objects encountered by the fish, thereby supporting the observed electrosense-dependent
123 spatial learning (Jun et al., 2016). Given the similar anatomical and functional organization of
124 visual and electrosensory motion pathways, we hypothesize that the transformation of
125 electrosensory motion signals to a spatial map are processed in DL. Here, we studied the
126 biophysical properties of DL neurons *in vitro* to determine whether their intrinsic properties are
127 compatible with their putative role in converting temporal input from PG (*i.e.*, time between object
128 encounters) to a spatial map (Wallach et al., 2018).

129

130 **Materials and methods**

131

132 For the following experiments, we used two closely related *Apteronotid* fish of either sex
133 (*A. leptorhynchus* and *A. albifrons*), a suborder of the gymnotiform family, as well as *Carassius*
134 *auratus* (goldfish) of either sex. The brains of *A. leptorhynchus* and *A. albifrons* cannot be readily
135 distinguished; these species have been used interchangeably in previous anatomical studies (e.g.,
136 Carr et al., 1982) and the processing of electrosensory input appears to be nearly identical in these
137 species (Martinez et al., 2016). Goldfish were included in this study for three reasons: First, we
138 found that *Apteronotus* DL cells were challenging to maintain in slice preparation, whereas
139 goldfish DL cells were more robust, yielding higher success rates on our lengthier protocols
140 involving pharmacological manipulations. Second, we wanted to check how our results
141 generalized to non-electrosensory teleosts, given the very general mechanisms of sparse neural
142 coding proposed in this article. Last, the critical behavioral experiments on the essential role of
143 DL in spatial memory were done in goldfish (Rodriguez et al., 2002), setting a precedent in the
144 literature; further, the first *in vivo* DL recordings have also been carried out in goldfish (Vinepinsky
145 et al., 2018). As demonstrated in the results, our conclusions apply equally well to each of these
146 species and are therefore directly relevant to spatial learning across a broad range of teleost fish.

147

148 Prior to use, the *Apteronotus* fish were kept in heated aquariums at 28°C, while goldfish
149 were kept in aquariums at 22°C (room temperature). All procedures were approved by the
150 University of Ottawa Animal Care Committee and follow the guidelines issued by the Society for
151 Neuroscience.

152

153 **Slice preparation.** Prior to the dissection, adult male and female fishes were anesthetized
 154 in oxygenated water containing 0.2% 3-aminobenzoic ethyl ester (tricaine methanesulfonate, Aqua
 155 Life, Syndel Laboratories, Canada). As the skull was being removed, ice cold oxygenated (95%
 156 O₂, 5% CO₂) artificial cerebrospinal fluid (ACSF: 130 mM NaCl, 24 mM NaHCO₃, 10 mM
 157 Glucose, 2.5 mM KCl, 1.75 mM KH₂HPO₄, 1.5 mM CaCl₂, 1.5 mM MgSO₄, 295 mOsm, pH 7.4),
 158 containing 1 mM of kynurenic acid (Millipore Sigma, Canada), was dripped onto the fish's brain.
 159 The brain was then carefully removed and submerged in a petri dish containing ice-cold ACSF
 160 with kynurenic acid. Once the brain was removed, it was placed in an ice-cold cubic mold, to
 161 which oxygenated ACSF mixed with 2.5% low-melting agarose (Millipore Sigma, Canada) was
 162 added. After the agarose has solidified, an initial cut was performed in order to separate the
 163 telencephalon from the rest of the brain. Subsequently, 300 µm thick coronal brain slices of the
 164 telencephalon were obtained using a vibratome. For goldfish dissections, a slightly different
 165 cutting ACSF was used (in mM): 108 NaCl, 24 NaHCO₃, 10 Glucose, 2.5 KCl, 1.25 KH₂HPO₄,
 166 1.5 CaCl₂, 1.5 MgSO₄, 2 HEPES, 260 mOsm. Furthermore, the thick optic nerves underneath the
 167 brain had to be severed with micro scissors before the brain was removed and placed in a petri dish
 168 containing ice-cold ACSF. The rest of the dissection was done in the same manner as in
 169 *Apteronotus*. Brain slices containing the dorsal lateral telencephalon (DL) were then transferred
 170 into a continuously oxygenated slice incubation chamber containing ACSF where they were left
 171 to rest for 30-60 minutes.

172

173 **In vitro recordings.** After the incubation period, brain slices containing DL were
 174 transferred to the recording chamber where oxygenated ACSF was constantly perfused at a flow
 175 rate of 3 mL/min. Recordings were performed at room temperature (23-24°C). We used fire-

176 polished borosilicate glass micropipettes (Sutter Instruments, CA) with resistances ranging
177 between 8-14 M Ω . The intracellular solution contained (in mM): 130 K-Gluconate, 10 KCl, 10
178 HEPES, 4 NaCl, 4 Mg-ATP, 10 phosphocreatine, 0.3 Na-GTP, with an osmolality of 295 mOsm,
179 and a pH of 7.2 for weakly electric fish recordings. A silver wire plated with silver chloride was
180 used as a ground. For goldfish experiments, recordings were done in the goldfish ACSF as
181 described above and a slightly different intracellular solutions was used (in mM): 110 K-
182 Gluconate, 10 KCl, 18 HEPES, 4 Mg-ATP, 10 phosphocreatine, 0.3 Na-GTP, 265mOsm, pH 7.2
183 . To visualize the neurons, slices were imaged under differential interference contrast (DIC) optics
184 using a CMOS infrared camera (Scientifica, UK) directly connected to the rig computer. The
185 recording signals were amplified using a Multiclamp 700B (Molecular Devices, CA), while the
186 signal was filtered at 3 kHz and digitized using a Digidata 1550 (Molecular Devices, CA). The
187 whole-cell recording data was acquired using the PClamp 10.6 software (Molecular Devices, CA,
188 RRID: SCR_011323). All recordings were performed in current-clamp mode. Only cells that
189 required a minimal holding current less than -50 pA were included in the study, allowing to
190 stabilize the cell near the average resting membrane potential (approximately -75 mV, see Fig.
191 2E). The maximal recording time after the dissection was 4-5 hours. Once the whole-cell
192 configuration was obtained, the resting membrane potential was recorded for 10 seconds and the
193 cells were injected with current steps, which typically range from 500 to 1000 ms and from -60 to
194 +60 pA, except where otherwise noted. For our ramp current protocol, we injected two different
195 ramp currents at different inter-stimulus time intervals ranging from 50 to 1000 ms. Although both
196 ramp stimuli have the same slope, the first ramp current was always two-fold stronger than the
197 second ramp since the first ramp current had to evoke multiple action potentials while the second
198 one only had to evoke one action potential. As such, the magnitude of the second current injection

199 had to be adjusted for each cell since the rheobase for each cell is different and the magnitude of
 200 the first ramp was then adjusted according to the second ramp. Healthy cells were usually held for
 201 30 to 60 minutes.

202

203 **Pharmacology.** A subset of DL cells exhibited membrane ‘noise’. We bath applied the
 204 non-selective antagonist, kynurenic acid (10 mM; Millipore Sigma, Canada), to block ionotropic
 205 glutamatergic transmission in order to determine whether this noise was due to synaptic input to
 206 DL cells.

207 To test for the presence of fast and persistent sodium channels in DL neurons, we first
 208 patched the cell and injected a standard 500 ms current step before applying 20 μ M TTX
 209 (Tetrodotoxin; Abcam, MA) locally near the recording site by pressure injection. To further
 210 investigate the presence of a persistent sodium channel, we also applied 5 mM QX-314 (Lidocaine
 211 N-ethyl bromide; Millipore Sigma, Canada) via the intracellular recording solution in order to
 212 block sodium (Salazar et al., 1996) and other channels (e.g., certain K^+ channels and Ca^{2+} channels,
 213 see Results) (Alreja and Aghajanian, 1994; Perkins and Wong, 1995; Talbot and Sayer, 1996).

214

215 Calcium-activated potassium channels SK1/2 are both expressed in DL. We used our
 216 standard current step protocol to evoke spikes in patched DL cells and bath applied an SK channel
 217 blocker 30 μ M UCL (6,12,19,20,25,26-Hexahydro-5,27:13,18:21,24-trietheno-11,7-metheno-7H-
 218 dibenzo [*b,n*] [1,5,12,16] tetraazacyclotricosine-5,13-dium dibromide; Tocris, Bio-Techne,
 219 Canada). We also locally applied 1 mM EBIO (1-Ethyl-2-benzimidazolinone; Abcam, MA), a SK
 220 channel agonist near the brain slice by pressure injection. Finally, we patched neurons using a
 221 slightly altered internal solution that contained 10 mM BAPTA (Millipore Sigma, Canada) in order

222 to chelate intracellular calcium. The osmolarity of this intracellular solution was readjusted to 295
 223 mOsm.

224

225 **RT-PCR.** G protein-coupled inwardly-rectifying potassium channels (GIRK) 1-4 mRNA
 226 sequences were identified from *A. leptorhynchus* brain transcriptome data (Salisbury et al., 2015).
 227 Two degenerate PCR primers were designed to bind all GIRK isoform sequences (Forward:
 228 CTGGTGGACCTSAAGTGGMG; reverse: TTCTTGGGCTGNGNAGATCTT). Five *A.*
 229 *leptorhynchus* fish were anesthetized with tricaine methanesulfonate (Aqua Life, Syndel
 230 Laboratories, Canada) and then sacrificed by cervical dislocation while being fed oxygenated
 231 water containing the anesthetic. Different regions of the brain (DL, tectum/torus, subpallium,
 232 cerebellum, ELL, hindbrain) were dissected in ice-cold ACSF, collected and preserved on dry ice.
 233 All tissues were weighed, and homogenized in Trizol to purify total RNA (Millipore Sigma,
 234 Canada). First-strand cDNAs were then generated by using the RevertAid H Minus First Strand
 235 cDNA Synthesis Kit (Fermentas, MA). Degenerate polymerase chain reaction (PCR) was
 236 performed using the DreamTaq, according to the manufacturer recommendations (Thermo Fisher
 237 Scientific, MA), with the primers mentioned above. On an agarose gel, the amplicon expected
 238 bands were 344bp.

239

240 **Data analysis.** All the recording data was first visualized in Clampfit (Molecular Devices,
 241 MA) before being transferred into Matlab (Mathworks, MA, RRID: SCR_001622) for subsequent
 242 analysis with custom scripts. To reduce the likelihood of analysing unhealthy cell responses, only
 243 cells which produced spikes that cross a data-driven threshold of -5mV were included in the
 244 analysis. Cells that showed significant membrane noise, *i.e.*, a variance greater than 0.5 mV^2 , were

245 used to construct Fig. 2G but were excluded from any additional analysis. For the analysis of the
246 resting membrane potential (Figure 2), only cells that did not require a holding current to stabilize
247 were included in this analysis. For the analysis of the average RMP (and variance) in Fig.3, a total
248 of 2 minutes of recording (binned into 10s sweeps) were analyzed for each cell before and after
249 the addition of the synaptic blocker (for a total of 4 minutes per cell). If the recording trace
250 contained any spontaneous action potentials, the action potentials were replaced with the
251 membrane potential recorded in the prior 100 ms. The membrane time constant was measured by
252 fitting an exponential function to the neuron's recovery to equilibrium following injection of a
253 negative step current. The spike amplitude was measured by two methods: first, as the difference
254 between the spike height and the spike threshold and, second, from the difference between the
255 spike height and the resting membrane potential. In order to estimate the spike threshold, we used
256 the method of Azouz et al. (2000) which defined the spike threshold as the voltage corresponding
257 to an empirically defined fraction (0.033) of the peak of the first derivative. This first derivative
258 method was later shown to be slightly better than the second derivative method (Sekerli et al.,
259 2004). The threshold for the broad Ca^{2+} spikes were determined visually in Clampfit since the rate
260 of change of the Ca^{2+} spike was too slow to be visualize with either the 1st or 2nd derivative of the
261 membrane potential. The spike width was calculated by measuring the half-width at half-
262 maximum. The voltage, as a function of injected current (I-V curves), was obtained in Clampfit
263 using sub-threshold traces and averaged in order to reduce the variability across cells caused by
264 the holding current. The input resistance was obtained by calculating the average slope of the I-V
265 curve across all cells. The after-hyperpolarization potential (AHP) amplitude was measured as the
266 difference between the spike threshold and the minimum value of the AHPs. If the recording trace
267 contained a burst or spike doublet, then the AHP would be measured on the following spike, since

268 a doublet would typically induce an especially large AHP. The cell's average firing rate was
 269 calculated as the number of spikes divided by the duration of the stimulus. The delta spike height
 270 was calculated as the difference in spike height between the n^{th} spike and the first spike of an
 271 evoked spike train. The inter-spike interval (ISI) was measured as the time between the first two
 272 spikes of the spike train induced by a current step injection, while the delta time was calculated as
 273 the difference between the time of the first AHP and the time of the n^{th} AHP. The delta AHP was
 274 obtained by subtracting the first spike's AHP amplitude from the second spike's AHP amplitude.
 275 The delta threshold was obtained in a similar fashion. All error bars were determined using the
 276 standard error of the mean. Wherever applicable, the statistical significance was determined using
 277 either one-way ANOVA, two-way ANOVA, one sample t-test, two sample t-test or the paired t-
 278 test, where $p < 0.05$ is considered significant.

279
 280 **Inactivating exponential integrate and fire model (iEIF).** In order to illustrate the
 281 putative role of slow sodium channel inactivation on the observed and variable spike threshold in
 282 DL cells, we sought a minimal neuron model that incorporates an abstraction of sodium channel
 283 dynamics. The inactivating exponential integrate and fire neuron (equation [1]; Platkiewicz and
 284 Brette, 2011) provides a distilled representation of sodium channel activation via an exponential
 285 amplification of the membrane voltage (V), which is attenuated by fast and slow inactivation
 286 variables (h_f and h_s). These sodium channel inactivation terms further affect the dynamic
 287 threshold for spike generation, θ , whose initial value V_r reflects no inactivation at the resting
 288 membrane potential (equation [2] and [3]; $h_f = h_s = 1$) (Platkiewicz and Brette, 2010). Although
 289 the exponential approximation does not realistically capture the full action potential waveform,
 290 which spans a large voltage range, it is valid for voltages near spike initiation. Importantly, this

approximation permits the differential equation for the variable spike threshold, θ , to be simply expressed by sodium channel properties described in equations [2] and [3] (Platkiewicz and Brette, 2010, 2011).

$$C \frac{dV}{dt} = g_L h_f h_s e^{\frac{V - V_T}{k_a}} + g_L (E_L - V) + I \quad \text{for } V < V_T \quad [1]$$

$$\theta = V_T - k_a \log(h_f h_s) \quad [2]$$

$$V_T = V_a - k_a \log\left(\frac{g_{Na}}{g_L} \frac{E_{Na} - V_a}{k_a}\right) \quad [3]$$

As in the work of Platkiewicz and Brette (2011), the membrane time constant, $\tau = C / g_L = 5$ ms, was introduced for our simulations. Given that the specific membrane capacitance is about 0.9 $\mu\text{F}/\text{cm}^2$ for practically all neuron types (Gentet et al., 2000), the leak conductance is constrained to be $g_L = 0.18$ mS/ cm^2 and the input current, $I = 3.8$ nA, is scaled by the associated membrane resistance (5.56 M Ω). The leak current reversal potential was set to $E_L = -55$ (Platkiewicz and Brette, 2011). When the membrane voltage reaches θ at time t , a spike is generated and $V(t^+)$ is reset to the resting membrane potential, $V_r = -70$ mV. The average threshold for the first spike in DL neurons was -42.96 ± 0.5 mV ($N = 42$ spikes). To obtain an approximate match between V_T and this value, we kept the sodium activation slope, $k_a = 4$ mV, and reversal potential, $V_a = -38.6$ mV, at the empirically justified values used by Platkiewicz and Brette (2011). We then set the sodium conductance to $g_{Na} = 0.036$ mS/ cm^2 to achieve a value of $g_{Na}/g_L = 0.2$, near the range of Platkiewicz and Brette (2011). We assume this slightly lower value in our model is a reflection of low sodium channel density. Consistent with this assumption, DL neuron axons are very thin and possibly unmyelinated (Giassi et al., 2012c) suggesting that they have a low sodium channel density, which may partly explains the high DL neuron threshold. The sodium channel reversal

312 potential was kept at a standard $E_{Na} = 50$ mV. When substituted into equation [3], the above
 313 parameter set yielded an initial threshold of $V_T = -44.6$ mV (Fig. 8E; ii) and gave particularly close
 314 agreement with the *Apterionotus* data (-44.5 ± 0.2 mV; Fig. 4E).

315

316 Drawing on the Hodgkin-Huxley formalism, the inactivation variables, h_f and h_s , evolve
 317 according to equations [4-5], where h_∞ is a Boltzmann equation with inactivation parameters V_i
 318 $= -63$ mV and $k_i = 6$ mV [6]:

$$319 \quad \tau_f \frac{dh_f}{dt} = h_\infty(V) - h_f \quad [4]$$

$$320 \quad \tau_s \frac{dh_s}{dt} = h_\infty(V) - h_s \quad [5]$$

$$321 \quad h_\infty(V) = \left(1 + e^{\frac{V - V_i}{k_i}} \right)^{-1} \quad [6]$$

322 The parameters τ_f (fast inactivation timescale) and τ_s (slow inactivation timescale) are of
 323 particular interest to the model and to our results. To determine τ_f , the average time between a
 324 short burst of two DL spikes (doublet) was measured at the beginning of the recorded voltage trace,
 325 yielding 15.38 ± 0.6 ms ($N = 144$ doublets). Selecting $\tau_f = 15$ ms, we note that the model
 326 generates spikes at a frequency of 64.7 ± 7.8 Hz, consistent with the data mean. We assumed that
 327 a slow timescale of inactivation would lead to an increase of spike threshold with a
 328 correspondingly long timescale for recovery (see Discussion). To select τ_s , we therefore noted
 329 that the threshold for DL cell spiking remains significantly increased for at least 300 ms when
 330 stimulated; therefore, τ_s is likely on the order of 10^2 milliseconds. A more direct estimate gave a

331 mean decay time constant (τ_{exp}) of ~640 ms for the slow recovery (see ramp protocol results
332 below). Therefore, we selected $\tau_s = 500$ ms, which is a conservative value, given slow
333 inactivation is typically >1 s and longer timescales would only further strengthen our hypotheses
334 (Itskov et al., 2011).

335

336 Note that we omitted Ca^{2+} currents and the resulting SK channel mediated AHP since its
337 duration is less than the typical interspike interval of DL neurons. When simulating the model,
338 subthreshold Gaussian noise, $N(0,1)$, was added to equation [1] and scaled by a factor $\sigma = 0.5$.
339 The stochastic forward Euler method was used as the numerical solver.

340

341 **Code Accessibility.** The Matlab code used in this paper is available as Extended Data and
342 at the University of Ottawa's Institutional repository with the corresponding DOI:
343 10.20381/ruor39306. A Windows 10 computer was used to simulate the results from the iEIF
344 model.

345

346 All panel figures were initially compiled in OriginPro 9.0 (OriginLabs, MA, RRID:
347 SCR_015636) and the final figures were assembled in Adobe Illustrator CS6 (Adobe Systems,
348 CA, RRID: SCR_010279).

349

350 Results

351

352 We performed whole cell patch recordings from *Apteronotus* DL neurons in acute slices
353 from the rostral- to mid-telencephalon (Fig. 1A). Cells within DL, imaged under infrared
354 illumination with DIC optics, had a shape and size consistent with those identified in Nissl stained
355 sections (Fig. 1B, C). Although we cannot differentiate between excitatory and inhibitory cells,
356 we assume that the neurons whose biophysical properties we characterize are almost certainly
357 those of excitatory (glutamatergic) DL neurons since they vastly predominate over the
358 rare inhibitory (GABAergic) cells (Giassi et al., 2012c). We also recorded neurons from the dorsal
359 portion of *Carassius auratus* (goldfish) DL, while avoiding the ventral DL as it receives olfactory
360 bulb input (Northcutt, 2006). The physiology of neurons recorded in the goldfish DL was not
361 distinguishable from those of *Apteronotus* (see below).

362

363 ‘Noisy’ versus ‘quiet’ cells

364 After attaining the whole-cell patch configuration, we first examined the resting membrane
365 potential (RMP, no holding current), and observed two distinct electrophysiological profiles. The
366 majority of the DL cells (29/35 cells in *Apteronotus* and 7/11 cells in goldfish) were ‘quiet’, that
367 is, they had minimal spontaneous membrane fluctuations, as shown by the example recording
368 traces from three different *Apteronotus* DL cells with different RMPs (Fig 2A). A smaller number
369 of DL neurons were ‘noisy,’ showing considerable spontaneous membrane fluctuations over
370 approximately the same range of RMPs as the ‘quiet’ cells (Fig 2B). A histogram estimating the
371 distribution of RMP variance (Fig. 2C) suggests that, in both *Apteronotus* and goldfish DL, there
372 were distinct populations of quiet (variance $< 0.5 \text{ mV}^2$) and noisy cells (variance $> 0.5 \text{ mV}^2$).

373

374 **Noisy cells.**

375 The ‘noisy’ electrophysiological feature has previously been observed in pyramidal cells
 376 in the *Apteronotus* hindbrain electrosensory lobe (ELL) and has been attributed to the stochastic
 377 opening of voltage-gated ion channels, an effect which becomes stronger as the membrane
 378 potential increases toward threshold (Marcoux et al., 2016). We therefore wondered whether noisy
 379 DL cells shared these features. DL neurons displayed an *in vitro* RMPs that were relatively more
 380 hyperpolarized (*Apteronotus*: -70 mV to -84 mV; goldfish: -66 mV to -78 mV; Fig 2D), compared
 381 to the ELL pyramidal cells (-67.8 ± 5.7 mV, Berman and Maler, 1998a) and neither subthreshold
 382 depolarizing, nor hyperpolarizing current steps altered the noise fluctuations of *Apteronotus* DL
 383 cells (N = 3 noisy cells; Fig. 2E). Additionally, we found that a more depolarized RMP of these
 384 noisy cells (*Apteronotus*, N = 6 cells; goldfish, N = 4 cells) was not associated with an increase in
 385 noise variance (Fig. 2F).

386 In some ‘noisy’ cells, spontaneous membrane fluctuations could summate to cause a more
 387 sustained depolarization (Fig. 3A). The summing fluctuations were usually between 10 and 20
 388 mV in amplitude and often induced spontaneous action potentials as the membrane potential
 389 crossed the spike threshold. The duration of these spontaneous events was estimated to be $425.5 \pm$
 390 42.4 ms (N = 4 cells), and could reach as long as 800 ms in instances where spontaneous bursting
 391 occurred (Fig. 3B). We hypothesize that these events are caused by the summation of multiple
 392 postsynaptic potentials, as highlighted by the arrows in Fig. 3C.

393 The intrinsic membrane noise of ELL pyramidal cells in the *Apteronotus* was shown to
 394 unaffected by AMPA(CNQX) and NMDA (APV) receptor antagonists (Marcoux et al., 2016); this
 395 was expected given the lack of recurrent connections in ELL (Maler, 1979; Maler et al., 1981). In

396 contrast, the application of kynurenic acid (10 mM), a broad spectrum AMPA/NMDA-R
 397 antagonist, completely blocked the membrane potential fluctuations of DL cells (*Apteronotus*: N
 398 = 3; goldfish: N = 2 cells; Fig.3D); the average variance of the membrane potential decreased from
 399 $2.8 \pm 0.9 \text{ mV}^2$ to $0.10 \pm 0.04 \text{ mV}^2$ (paired t-test; $p = 0.0383$; Fig. 3E) while having a negligible
 400 effect on the average resting membrane potential (paired t-test; $p = 0.7372$; Fig. 3F).

401 Based on these observations, we suggest that the DL cell membrane noise, are not
 402 generated by intrinsic conductances, but are instead primarily due to synaptic bombardment from
 403 neighboring cells within the DL recurrent network (Trinh et al., 2016). In our slice preparation,
 404 DL is disconnected from all extrinsic input (Giassi et al., 2012b; Giassi et al., 2012a). As such, the
 405 synaptic noise we observed in a subset of DL neurons provides evidence that the activity of the
 406 DL recurrent network alone can drive weak spiking activity. We do not currently know why only
 407 some neurons show pronounced membrane potential fluctuations.

408

409 **Quiet Cells**

410 **Resting membrane potential, spike threshold and spike discharge patterns**

411 The RMPs of quiet *Apteronotus* DL cells were approximately Gaussian distributed with a
 412 mean of $-76.7 \pm 0.3 \text{ mV}$ (N = 29 cells, Fig. 2D), similar to that of goldfish ($-74.4 \pm 0.7 \text{ mV}$, N = 7
 413 cells). Using the hyperpolarized responses to negative current steps, we calculated an average
 414 membrane time constant of $10.28 \pm 0.24 \text{ ms}$ for these neurons.

415

416 We next injected positive current steps in order to generate spiking. An example recording
 417 is shown in Fig. 4Ai, illustrating a typical DL neuron response in *Apteronotus*. The same response
 418 and spiking pattern was found in all cells regardless of their location within the *Apteronotus* DL

419 region and was also observed in the goldfish DL (Fig. 4B). DL neurons exhibited very pronounced
 420 rectification: the membrane potential deflection in response to depolarizing current injections was
 421 far stronger than for hyperpolarizing currents of the same magnitude (Fig. 4Aii). This asymmetry
 422 is quantified below. In addition, we never observed any ‘sags’ in the response of DL neurons to
 423 hyperpolarizing current injections, suggesting that they do not express hyperpolarization-activated
 424 cation channels (I_h).

425
 426 DL neurons discharge very few action potentials (Figs. 4A, B) and the average injected
 427 current necessary to reach spike threshold (rheobase) was 38.17 ± 2.52 pA (N=15 cells). Strong
 428 current injections (70 pA) only resulted in average firing rates of 15.3 ± 2.4 Hz (N = 15 cells). We
 429 defined the spike threshold as the voltage corresponding to a pre-determined fraction of the
 430 maximal peak of the first derivative of the membrane potential response to current steps (Azouz
 431 and Gray, 2000; methods). Strong current injection in *Apteronotus* DL neurons typically results in
 432 an initial high frequency burst of 2 or 3 spikes, followed by an irregular series of spikes separated
 433 by AHPs of varying amplitude and duration (Figs. 4C, D); the same pattern was also observed in
 434 the DL of goldfish (Fig. 4B and 5A). In *Apteronotus*, the threshold for the first spike is distributed
 435 with a mean of -45.3 ± 0.2 mV (N = 22 cells) and has a high degree of overlap with the observed
 436 spike threshold for goldfish DL cells (mean: -41.5 ± 0.3 mV, N = 14 cells; Fig. 4E). We measured
 437 the mean spike peak amplitude from both the membrane potential at spike threshold (*Apteronotus*:
 438 66.2 ± 1.0 mV, N = 22 cells; goldfish: 50.8 ± 1.0 mV, N = 14 cells) and from the RMP
 439 (*Apteronotus*, 95.9 ± 0.5 mV; goldfish, 90.6 ± 0.5 mV). Lastly, we also measured the spike half-
 440 width at half-maximum (*Apteronotus*: 2.3 ± 0.1 ms; goldfish: 3.7 ± 0.3 ms).

441

442 In summary, the core biophysical properties of DL cells receiving PG input in *Apteronotus*
443 and goldfish (dorsal DL, non-olfactory, Northcutt, 2006; Yamamoto and Ito, 2005) were similar -
444 DL neurons have a hyperpolarized RMP and a high spike threshold and spike only sparsely in
445 response to even strong current injection.

446

447 **Asymmetric input resistance**

448 A striking property of *Apteronotus* and goldfish DL cells is an asymmetry in their response
449 to hyperpolarizing versus depolarizing current steps (Fig.5Ai). In ELL pyramidal cells, an
450 equivalent, though far smaller asymmetry is caused by a persistent Na⁺ channel (Turner et al.,
451 1994) that amplifies excitatory synaptic input (Berman et al., 2001). We tested this possibility by
452 blocking the sodium channels of DL neurons with a local application of 20 μ M TTX (control: N
453 = 18 cells, TTX: N = 6 cells). As expected, spike discharge at the previous threshold (\sim 45 mV)
454 was completely blocked by TTX (Fig. 5Aii); the small high-threshold spikes evoked with much
455 stronger current injections will be discussed below (Fig. 5Aii, Cii). Upon closer inspection of the
456 neurons' response to positive current injections, we found that application of TTX did not
457 dramatically change their depolarizing ramp response to peri-threshold current injection (Fig. 5Bi)
458 and, in some cases, would even slightly increase the neuron's response to positive current
459 injections (Fig. 5Bii). This data indicates that low threshold persistent sodium channels are likely
460 not (or only weakly) expressed in DL neurons.

461

462 We next plotted the average I-V curves for negative and positive (subthreshold) current
463 injection (*Apteronotus* and goldfish, Fig. 5D). The stronger response to positive versus negative
464 current injection can be clearly seen in the rectification of the I-V curve for the control condition.

465 These curves can be used to compute separate input resistances for positive and negative current
 466 injections. Typically, the response to hyperpolarizing current injection is assumed to reflect the
 467 passive properties of a neuron and is reported as its input resistance (e.g., ELL pyramidal cells;
 468 Mathieson and Maler, 1988; Berman et al., 1997). In DL cells, the input resistance for depolarizing
 469 current injection is approximately double that for hyperpolarizing current injection when compared
 470 under both control and TTX conditions (Table 1; paired t-test; control; $p = 3.3 \times 10^{-12}$, TTX; $p =$
 471 9.9×10^{-6}). The addition of TTX had no significant effect on the hyperpolarizing slope (one way
 472 ANOVA; $p = 0.32$), nor did it have any significant effect on the input resistance for the
 473 depolarizing slope (Table 1: one way ANOVA; $p = 0.42$; Fig. 5D). Thus, it appears that there is
 474 no contribution of persistent Na^+ channels to the resting membrane potential of DL neurons, in
 475 accordance with the small effects of TTX observed in Fig. 5B.

476
 477 To further investigate the basis of the observed asymmetrical response to current injection,
 478 we have also recorded DL neurons using an intracellular solution containing 5 mM QX-314, a
 479 blocker of Na^+ channels, as well as some K^+ and Ca^{2+} channels (Talbot and Sayer, 1996) (Fig. 5C,
 480 D; control, $N = 18$ cells; QX-314, $N = 6$ cells). QX-314 has previously been used to block all Na^+
 481 channels in *Apterionotus* ELL pyramidal cells (Berman et al., 2001). The I-V graph constructed
 482 from the QX-314 experiments showed a higher depolarizing versus hyperpolarizing input
 483 resistance (paired t-test; $p = 2.3 \times 10^{-4}$), similar to control and TTX conditions (above). There was
 484 a small increase in input resistance for the depolarizing current injection that failed to reach
 485 significance (Table 1: one way ANOVA, $p = 0.07$; Fig. 5D). In contrast, there was a large and
 486 highly significant increase of input resistance in the responses to hyperpolarizing current injections
 487 – it more than doubled over control values (Table 1: one way ANOVA, $p = 5.9 \times 10^{-5}$). Since we

only expect K^+ permeating channels to be open at such hyperpolarized membrane potential, we attribute this effect to the ‘non-specific’ actions of QX-314 (Perkins and Wong, 1995; Slesinger, 2001). The results of the TTX and QX-314 experiments lead to two hypotheses: first, the subthreshold response of DL cells to depolarizing input is mainly due to their passive membrane properties. Second, the RMP of hyperpolarized DL cells is likely due to a strong rectifying K^+ conductance that is blocked by QX-314 and typically prevents the cell from deviating from the reversal potential of K^+ ions (Fig. 5). Given that GIRK channels are ubiquitous in the mammalian cortex (Luscher and Slesinger, 2010; Lujan and Aguado, 2015) and can be blocked by QX-314 (Zhou et al., 2001), we suspected them to also be present in the teleost pallium. To confirm the presence of GIRKs in DL, we used a RT-PCR approach to show the expression of GIRK channels in different brain regions in the *Apteronotid* fish (DL, subpallium, tectum/torus, cerebellum, ELL and hindbrain) using a primer pair hybridizing in conserved segments of all GIRK paralogs. Unsurprisingly, pan-GIRK amplicons were found in all brain regions, but were not present in the control (Fig. 5-2) suggesting that GIRK channels are ubiquitously expressed in the *Apteronotus* brain.

Voltage dependent calcium conductance

In the presence of TTX, strong current injections (>80 pA) were able to evoke a broad (half-width: 33.0 ± 3.1 ms) spike with a very high threshold (mean threshold: -21.2 ± 0.5 mV, $N = 4$ of 6 cells; Fig. 5Aii). Spike amplitude was 18.6 ± 0.7 mV from the threshold potential and 79.1 ± 0.9 mV from the RMP. Similar to the TTX results, QX-314 treated cells did not produce any action potentials at the threshold for control cells (Fig. 5Ci), but did produce broad spikes at much higher stimulus intensities (spike half-width; 21.1 ± 1.1 ms; height = 31.3 ± 0.7 mV from threshold

511 and 100.6 ± 0.9 mV from RMP, $N = 4$ of 6 cells, Fig. 5Cii). The average threshold for these broad
 512 spikes was found to be at -6.8 ± 1.3 mV, which is also consistent with the range of voltages that
 513 has been reported for the activation of HVA Ca^{2+} channels (Tsien et al., 1988). Therefore, we
 514 hypothesize that DL neurons express HVA Ca^{2+} channels that will likely be activated by Na^{+}
 515 mediated action potentials.

516

517 **After-hyperpolarizing potentials**

518 DL neurons exhibit a strong AHP (Figs. 4-6). Previously, it was shown that DL cells
 519 express both SK1 and SK2 channels (Ellis et al., 2008) and that UCL1684 is highly effective at
 520 blocking such channels (Harvey-Girard and Maler, 2013). We therefore bath-applied 30 μM
 521 UCL1684, resulting in a significantly diminished AHP compared to the control conditions (Fig.
 522 6A). To quantify this AHP reduction, we measured the AHP amplitude (Fig. 6Ci) and the area
 523 under the AHP (Fig. 6Cii) following the first single spike obtained in response to current injection.
 524 The addition of UCL1684 reduced the average amplitude of the first AHP to half its control value
 525 (Fig. 6Ci: control: 3.5 ± 0.3 mV, $N = 13$ cells; UCL1684: 1.4 ± 0.2 mV; $N = 7$ cells; two sample
 526 t-test; $p = 0.0003$). A similar reduction was also observed when comparing the area under AHPs:
 527 from 1980.3 ± 192.6 mV \cdot ms to 701.4 ± 128.4 mV \cdot ms (Fig. 6Cii, two-sample t-test; $p = 0.0002$).
 528 In contrast, after the addition of the SK channel agonist EBIO (1 mM; Ellis et al., 2007), current
 529 injection evoked very few spikes; thus current steps were increased to 750 ms and 1000 ms. As
 530 expected, the average AHP amplitude increased from 3.5 ± 0.3 mV to 6.7 ± 1.0 mV (control, $N =$
 531 13 cells; EBIO, $N = 6$ cells; two sample t-test; $p = 0.001$), while the area under the curve also
 532 increased from 1980.3 ± 192.6 mV \cdot ms to 3952.2 ± 277.5 mV \cdot ms (two sample t-test, $p =$
 533 0.00002).

534

535 Blocking SK channels also increased the current-evoked firing rate compared to the control
 536 condition (Fig. 6D; control, N = 28 cells; UCL1684, N = 7 cells; two-way ANOVA; $p = 0.0013$),
 537 while EBIO reduced the evoked firing rate since the cell required a longer time to reach spike
 538 threshold after the first spike (Fig. 6B, D; N = 6 cells; two-way ANOVA; $p = 0.000092$). We
 539 conclude that the SK1/2 channels of DL neurons act as negative feedback on the cell's
 540 responsiveness to excitatory input.

541

542 Finally, we wanted to confirm whether SK channel activation in DL neurons could be
 543 blocked by preventing Ca^{2+} activation of the channel. We recorded DL neurons in *Apteronotus*
 544 using an intracellular solution containing 10 mM BAPTA, a Ca^{2+} chelator (N = 7 cells; Fig. 7A).
 545 In all cases, the AHP was completely abolished, unlike the partial AHP block obtained with
 546 UCL1684. This suggests that another unidentified Ca^{2+} activated K^+ channel may also be
 547 contributing to the AHP. Further work will be required to investigate this possibility. The firing
 548 rate also dramatically increased compared to the control condition (control, N = 28; UCL1684, N
 549 = 7; BAPTA, N = 7 cells; Fig. 7B; two-way ANOVA; $p = 1.5 \times 10^{-15}$) and compared to UCL1684
 550 treatment (two-way ANOVA; $p = 0.00063$). Furthermore, this BAPTA-induced increase in firing
 551 rate was also accompanied by a significant reduction in spike height compared to both control
 552 (Fig. 7C; two-way ANOVA; $p = 2.1 \times 10^{-12}$) and UCL1684 conditions (two-way ANOVA; $p = 1.6$
 553 $\times 10^{-6}$). In contrast, the difference in spike height between the UCL1684 and control did not yield
 554 a significant difference (two-way ANOVA; $p = 0.14$). We hypothesize that Na^+ channel
 555 inactivation may be causing this reduction (see below). Another distinctive feature of the DL
 556 neuron's spiking response during the BAPTA application was the increase in spike width occurring

557 along successive spikes and typically becoming most prominent by the 8th spike (Fig. 7A, D). In
 558 the control and UCL1684 conditions, there was a slight increase in spike width, however, in the
 559 BAPTA condition, the spike width increased dramatically with successive spikes (Fig. 7A, 7D)
 560 compared to control (two-way ANOVA; $p = 1.3 \times 10^{-31}$) and UCL1684 conditions (two-way
 561 ANOVA; $p = 3.7 \times 10^{-10}$). In contrast, the difference between the control and BAPTA conditions
 562 was not significant up until the third spike (two-way ANOVA; $p = 0.24$), suggesting that the spike
 563 width increase is caused by a cumulative process. Calcium channels typically inactivate via a Ca^{2+} -
 564 dependent mechanism (Simms and Zamponi, 2014), leading us to hypothesize that this dramatic
 565 change in spike width may be caused by a decrease in Ca^{2+} -dependent inactivation of the Ca^{2+}
 566 channel leading to an increase of its open time.

567

568 **Dynamic AHP and spike threshold**

569 Although the presence of the AHP greatly reduces the firing rate, we also observed that
 570 after successive spikes, the AHP itself decreased (Fig. 8-2A) and the spike threshold increased
 571 (Fig. 8A). To better quantify the AHP modulation, we measured the difference in AHP amplitude
 572 between the first two spikes of a current-evoked spike train that did not show an initial burst. We
 573 found that there was a significant reduction in AHP amplitude that was invariant to the time length
 574 of the AHP (Fig. 8-2B black squares; $N = 26$ cells; one-sample t-test, $p = 4.45 \times 10^{-27}$). For recording
 575 traces that showed initial bursts, we examined the first spike pair following the burst and found a
 576 similar reduction in AHP (Fig. 8-2B, grey triangles; $N = 20$ cells; one sample t-test, $p = 1.26 \times 10^{-13}$).
 577 This reduction is presumably caused by Ca^{2+} -induced inactivation of the HVA Ca^{2+} channels,
 578 which will decrease the total amount of Ca^{2+} available to the cell and limit the activation of SK
 579 channels.

580

581 Even with the spiking-induced reduction of the AHP, DL neurons could not surpass a
 582 sustained firing rate of 30 Hz (Fig. 7B), which suggests the presence of an additional mechanism(s)
 583 that limits firing rate. In ELL pyramidal neurons, spike threshold fatigue has been shown to limit
 584 the firing rate whenever a burst occurs (Chacron et al., 2007). Upon closer inspection, we found a
 585 significant increase in spike threshold during long spike trains (Fig. 8A). This dynamic spike
 586 threshold was also found to be invariant to the inter-spike interval (up to ~300 ms) for both non-
 587 burst traces (Fig. 8B, black squares; one-sample t-test, $p = 1.24 \times 10^{-22}$) and for traces containing
 588 an initial burst (Fig. 8B; one sample t-test, $p = 8.30 \times 10^{-28}$). Next, we wanted to confirm whether
 589 the threshold fatigue that was observed in DL neurons may be caused by the history of past spikes,
 590 *i.e.*, whether Na^+ channel inactivation due to continuous spiking may influence the spike threshold.
 591 We examined the difference in threshold for all non-burst traces to see whether it varies throughout
 592 a spike train. The threshold increase continued to at least 10 spikes and could be fitted by a double
 593 exponential function (equation: $y = 2.72e^{0.04x} + -9.0e^{-0.72x}$; $R^2 = 0.987$; Fig. 8C); here we considered
 594 only the number of spikes and not the duration of the spike train. A similar analysis where the
 595 difference in threshold was compared to the time between spikes instead of the spike number also
 596 led to the same conclusion: this effect became more prominent after long periods of depolarization
 597 despite the variability in the number of intervening spikes (Fig. 8D). These results suggest that the
 598 increase in threshold is caused by an accumulation of slow Na^+ channel inactivation.

599

600 In mammalian cortical cells, the recovery from inactivation of Na^+ channels have both a
 601 fast component (millisecond timescale) and a slow component that can extend to much longer
 602 timescales (seconds to minutes; Fleidervish et al., 1996; Mickus et al., 1999; Ellerkmann et al.,

2001). To quantify the duration of this spike threshold adaptation, we developed a protocol in which a long ramp current (evoking multiple spikes) was injected followed by a shorter ramp current (evoking one spike) at various inter-stimulus time intervals (Fig. 9A, upper panel). This protocol induced spike threshold fatigue during the first current injection, while the second current injection was used to test for time-dependent changes in spike threshold. We found that the increase in spike threshold between the first and second current injection was significantly higher at short compared to longer time intervals (Fig. 9A, bottom panel). Using these changes in threshold, we found that the recovery from this spike threshold fatigue had a highly variable time constant ranging from 300 ms to 900 ms with an average time constant $\tau_{\text{exp}} = 637.28 \pm 85.9$ ms (Fig. 9B). This suggest that the decrease in cell excitability caused by the dynamic threshold can operate on the timescale of hundreds of milliseconds.

To further investigate whether Na^+ channel inactivation is responsible for the observed increase in threshold, we employed a model with minimal assumptions: the inactivating exponential integrate and fire model (Platkiewicz and Brette, 2011). This model includes a slow inactivation term, as well as the traditional fast inactivation term associated with Na^+ channels; inactivation kinetics for both forms were derived from our data (see Methods). Since we were primarily interested in the effect of sodium inactivation on the spike threshold, the minimal model omits AHP dynamics and Ca^{2+} currents (see Methods). We found that the addition of slowly inactivating Na^+ channels, as suggested by the effects of BAPTA (Fig. 7A), was itself sufficient to qualitatively reproduce the response of DL neurons to current injection and predict an increase in spike threshold that was similar to that observed in our whole-cell recordings (Fig. 9C). We therefore conclude that the accumulation of slow Na^+ channel inactivation, caused by spike

626 discharge and simple depolarization, may act as a source of negative feedback to reduce the cell's
627 firing rate via an increase in spike threshold.
628

629 Discussion

630

631 The work presented here is, to our knowledge, the first study of the biophysical properties
632 of teleost DL neurons. Our previous work mapped the local DL circuitry (Trinh et al., 2016), the
633 organization of thalamic and other inputs to DL (Giassi et al., 2012b), and the telencephalic
634 connectivity of DL (Giassi et al., 2012a; Elliott et al., 2017). In gymnotiform fish, we have
635 previously shown that the electrosensory system contributes to spatial learning (Jun et al., 2016),
636 and that the PG (thalamic) inputs to DL can encode responses to object motion (Wallach et al.,
637 2018). Although the intrinsic and extrinsic properties of DL synaptic input have yet to be
638 examined, we believe that the constraints imposed by DL circuitry, behavioural function plus
639 recent theoretical analyses, are sufficient to generate testable hypotheses of the computations
640 performed by DL during spatial learning. Below, we first summarize the main conclusions of our
641 work and then discuss whether the biophysical properties of DL neurons and their connectivity are
642 compatible with the critical role of DL in spatial learning and memory. In particular, we suggest
643 that DL neurons possess the minimal requirements to be labelled as sparse coders. Next, we
644 suggest that spike threshold adaptation is key to the extraction of spatial information in DL from
645 the time stamped electrosensory input conveyed by PG (Wallach et al., 2018). Our hypothesis
646 relies on a previous theoretical model of time coding cells (Itskov et al., 2008) that utilizes, as an
647 essential ingredient, spike threshold adaptation with a long recovery time constant.

648

649 Our main results show that DL neurons express a combination of ion channels that have
650 been reported for many other types of neurons. DL neurons have a hyperpolarized RMP. We
651 hypothesize that this is due, at least in part, to GIRK channels. GIRKs can hyperpolarize

mammalian CA1 hippocampal neurons by at least 8 mV under basal conditions (Luscher and Slesinger, 2010) and have been shown to set the RMP of dorsal cochlear nucleus neurons to a hyperpolarized level (Ceballos et al., 2016). DL neurons also have a high spike threshold and theoretical analyses suggest this may attributed to a low density of voltage-gated Na^+ channels (Platkiewicz and Brette, 2010). Furthermore, our results also imply the presence of HVA Ca^{2+} channels, which activate a strong SK channel mediated AHP that strongly reduces current-evoked spiking. We propose that the combination of a hyperpolarized RMP, the low input resistance at hyperpolarized potentials (Table 1), a high spike threshold and strong AHPs will greatly reduce DL cell excitability and therefore prevent incoming excitatory synaptic input from driving strong spiking responses.

An unusual and, we believe, critical feature of DL neurons is that they exhibit long-lasting spike threshold adaptation (*i.e.*, threshold fatigue); our modeling suggests that this is due to Na^+ channels exhibiting slow recovery from inactivation. In mammalian cortical neurons, the Na^+ channel's slow recovery from inactivation can last up to a few seconds and can regulate the neuron's excitability; in particular, the slow inactivation of dendritic Na^+ channels in CA1 neurons can attenuate back-propagating action potentials (Jung et al., 1997). In addition, the link between a sustained spike threshold increase and the slow inactivation of Na^+ channels has previously been suggested for hippocampal CA1 pyramidal neurons (Henze and Buzsaki, 2001). This spike threshold adaptation mechanism was later used to model time cells using a recurrent network model (Itskov et al., 2011, see below). We note that the AHP and slowly recovering Na^+ inactivation have very different effects on neuron excitability (Benda et al., 2010). The dynamical interaction of these biophysical mechanisms (not currently known) will likely be a critical

determinant of the spiking response of DL neurons to their time varying synaptic input. Developing a high quality model of DL cells will be an essential next step in connecting the dynamics of the DL recurrent network (Trinh et al., 2016) to *in vivo* imaging/recording and behavioral studies on spatial learning in the dark (Jun et al., 2016).

The biophysical properties of DL neurons suggest that they are sparse coders.

The main properties that contribute to low DL neuron firing rates are the very depolarized spike threshold and hyperpolarized RMP (Table 2); these parameters are highly variable but typically lead to a large (~32 mV) barrier that excitatory input must exceed to evoke spiking (Table 2). This contrasts sharply with the first order electrosensory pyramidal cells within the ELL. Their barrier from rest to spiking is a mere 4.9 mV (Table 2) and they can even respond to weak signals with discharge frequencies over 100 Hz. ELL pyramidal neurons also recover rapidly from spike induced increases in spike threshold, *i.e.*, threshold fatigue (10s of milliseconds, Chacron et al., 2007). It is hypothesized that these properties are responsible for the ability of pyramidal cells to densely encode spatial and social electrosensory signals (Vonderschen and Chacron, 2011). The low barrier from RMP to spike threshold is also seen in primary auditory neurons and in layer 4 cells of the primary visual and somatosensory cortex (Table 2). Although no precise estimates are available, it appears likely that all these low level sensory neurons encode sensory input much more densely than neurons in the hippocampus.

Hippocampal neurons such as dentate gyrus granule cells are nearly silent at rest, and discharge very sparsely in response to the animal's spatial location, *i.e.*, place field (Diamantaki et al., 2016). The low excitability in mature granule cells was shown to be partly due to the

698 constitutive activity of GIRK channels (Gonzalez et al., 2018). We hypothesize that a similar
699 mechanism is contributing to the low RMP of DL neurons in fish, which may partly explain why
700 the difference between RMP and spike threshold is nearly identical in DL and DG cells (Table 2).

701 With the above examples in mind, we hypothesize that the key biophysical signatures of
702 sparse coding is, for all neurons, a large gap between the RMP and the spike threshold. We further
703 hypothesize that DL neurons will sparsely encode the spatial relations required for memory guided
704 navigation.

705

706 **Can the DL network transform PG sequential encounter time stamps to a spatial map?**

707 Previous studies have investigated electrosensory spatial learning in a related gymnotiform
708 fish (Jun et al., 2016; Fotowat et al., 2019). Jun et al. showed that these fish can locate food relative
709 to landmarks in the dark because, after learning, they rapidly navigated to the remembered food
710 location during probe trials (no food). Fotowat et al. showed that neurons within DD, which has
711 strong reciprocal connections with DL (Giassi et al., 2012a; Elliott et al., 2016), discharged when
712 the fish was engaged in active sensing movements near landmarks. Together, these studies imply
713 that DL is engaged in learning and storing the spatial memories of the relative location of
714 landmarks and food. The electrosense is very local and, for most of their trajectory, the fish had
715 no external sensory cues (Jun et al., 2016). This led Jun et al. to argue that, after leaving a landmark,
716 the fish used the path integration of speed and orientation signals to continuously update its current
717 location and thus compute the trajectory to the remembered food location. Path integration
718 information was assumed to potentially derive from lateral line receptors, vestibular afferents,
719 proprioceptors and vestibular afferents. Bastian et al. (1995) has previously reported that there are
720 brainstem proprioceptive neurons in the gymnotiform fish that are capable of signalling tail

721 bending. Recently, Wallach et al. found PG neurons are responsive to continuous lateral line input,
722 confirming a second potential source of information related to the fish's speed. A recent study in
723 the larval zebrafish has demonstrated that vestibular input can evoked strong and widespread
724 activity in the telencephalon that, from the images presented, likely includes DL (Favre-Bulle et
725 al., 2018). We now hypothesize that an encounter with a landmark triggers an autonomous 'moving
726 bump' in the DL recurrent network and this is the primary driver for the fish's estimation of its
727 changing location during its landmark-to-food trajectories. While proprioceptive, lateral line and
728 vestibular input are important, we now hypothesize they merely modulate the essential intrinsic
729 DL network dynamics. We elaborate on this hypothesis below.

730

731 In gymnotiform fish, PG cells respond to object motion (electrosensory and visual; Wallach
732 et al., 2018). Anatomical studies indicate that these responses are driven by tectal input (Giassi et
733 al., 2011). The gymnotiform tectum maintains a topographic representation of electrosensory input
734 and tracks continuous object motion (Bastian, 1982). PG neurons generate a major transformation
735 of their tectal input - the majority of PG motion sensitive cells lose topographic information and
736 respond over the fish's entire body but only to object motion start (all cells) and stop (some cells)
737 and not the intervening continuous motion (Wallach et al., 2018). Wallach et al. proposed that,
738 during navigation in the dark, these PG cells will respond transiently when any part of the fish's
739 body first encounters a landmark (or food), *i.e.*, the response of the cell when the experimenter
740 moves an object towards the fish is equivalent to its response when the fish moves near a landmark
741 or food. Wallach et al. further proposed that the time interval between encounters could be 'read
742 out' from the change in second versus first encounter firing rates of a subset of DL cells.

743

744 In the following discussion, we borrow extensively from work on ‘time’ and ‘place’ cells
745 in the mammalian hippocampus using, in particular, the very thorough papers of Kraus et al. (2013)
746 and Pastalova et al. (2008) as well as the related theoretical papers of Itskov et al. (2011) and Rajan
747 et al. (2016). Kraus et al. describe hippocampal neurons that respond at specific times during a
748 rat’s motion on a treadmill. These experiments carefully dissociated time from place so that the
749 authors were able to demonstrate the existence of ‘time cells’, traditional place cells as well as
750 cells with information on both the time and distance travelled. Pastalkova et al. and Itskov et al.
751 had previously argued that sequential activation of cell assemblies is internally generated by
752 hippocampal dynamics and can give rise to time cells independent of sensory input. Kraus et al.
753 extended this hypothesis and argued that their time cells were driven by both internal network
754 dynamics and external cues such as treadmill speed.

755

756 The theoretical papers of Itskov et al. and Rajan et al. asked: how might the intrinsic activity
757 of a neural network result in the sequential activation of neuron assemblies, e.g., time cells? Both
758 papers started with the same core architecture – a local excitatory recurrent network that, once
759 activated, was capable of sustained discharge. This is the ‘bump attractor’ hypothesis originally
760 formulated to explain the sustained activity of neurons during a working memory task (Wang,
761 1999; Wimmer et al., 2014). The theoretical analysis of Wang (1999) demonstrated that slow
762 excitatory synapses, *i.e.*, mediated by NMDA receptors, were required for bump dynamics. Both
763 Itskov et al. and Rajan et al. generated ‘cell assembly sequences’ by destabilizing the bump
764 attractor dynamics. Itskov et al. accomplished this by introducing spike threshold adaptation with
765 a long recovery time constant. In contrast, Rajan et al. destabilized the bump by introducing
766 asymmetries in synaptic strengths within the attractor so that the attractor dynamics would generate

767 a sequential activation of the cell assembly; a process which necessitated both recurrent
768 connections and external input. In both cases, sequential activation of neurons within the cell
769 assembly are able to produce time cells or other sequential outputs. A recent paper (Heys and
770 Dombeck, 2018) has also suggested that ‘time cells’ of the entorhinal cortex might be generated
771 by moving bumps in entorhinal recurrent attractor network (Zutshi et al., 2018). This paper did
772 not, however, explicitly discuss the mechanism by which the putative ‘bumps’ would move.

773

774 Our earlier work (Trinh et al., 2016) demonstrated that DL contains excitatory local
775 recurrent networks; our earlier work had already demonstrated that DL is highly enriched in
776 NMDA receptors (Harvey-Girard et al., 2007). Trinh et al. therefore hypothesized that the DL
777 recurrent network supported bump attractor dynamics capable of memory storage. Our ‘noisy’
778 cells suggest that the recurrent connections within DL are, in fact, capable of supporting
779 autonomous discharge. We have now demonstrated that DL neurons exhibit the same threshold
780 adaptation utilized in the Itskov et al. model thus suggesting that the putative DL bumps may not
781 be stable attractors. We have not yet studied the properties of either PG-derived or intrinsic
782 synapses in DL and therefore cannot evaluate whether Rajan et al.’s architecture might apply. In
783 accordance with the Itskov model, we hypothesize that DL contains unstable bump attractor neural
784 networks that are capable of supporting autonomous sequential activation and thus DL time cells.
785 We assume that, when the fish initially encounters a landmark, the resulting electrosensory-evoked
786 transient discharge in a subset of PG neurons triggers activity in a small region of DL (Giassi et
787 al., 2012b). This activity will then propagate through a subset of the DL network forming a cell
788 assembly temporal sequence (time cells). Following Kraus et al., we further hypothesize that the
789 sequential activity in this network is modified by ongoing self-motion sensory input – the

790 vestibular, lateral line and proprioceptive input mentioned above. These inputs provide the path
791 integration signals that converts the time cell sequence to a location cell sequence. In functional
792 terms, we propose that the propagation of neural activity in the DL network represents the fish's
793 estimate of where it is located along the trajectory between a landmark and food. When the fish
794 reaches the food (or another landmark), PG neurons would again discharge to signal the total
795 time/distance travelled (Wallach et al., 2018) and the potential start of a new trajectory. In this
796 model, learning a trajectory from a particular landmark to food would consist of strengthening the
797 synaptic connections of the 'moving bump' induced by that landmark so as to represent the
798 time/location sequence leading from the landmark to food. Such strengthening might result in
799 Rajan et al. type mechanism in which directed bump movement was now also a consequence of
800 asymmetric synaptic strengthening.

801

802 Our hypotheses are at the moment not testable, because testing would require population
803 recording from or visualizing activity across a large portion of the DL network. What is needed is
804 a teleost that is transparent when adult, whose neurons express a genetically encoded calcium
805 indicator (e.g., gCamp6) and whose pallium might be activated by ethologically relevant transient
806 signals. Fortunately, such a model system has recently become available (Schulze et al., 2018) and
807 may permit direct tests of our hypotheses.

808

- Alreja M, Aghajanian GK (1994) QX-314 blocks the potassium but not the sodium-dependent component of the opiate response in locus coeruleus neurons. *Brain Res* 639:320-324.
- Azouz R, Gray CM (2000) Dynamic spike threshold reveals a mechanism for synaptic coincidence detection in cortical neurons in vivo. *Proc Natl Acad Sci U S A* 97:8110-8115.
- Barry C, Burgess N (2014) Neural mechanisms of self-location. *Curr Biol* 24:R330-339.
- Bastian J (1982) Vision and electroreception. Integration of sensory information in the optic tectum of the weakly electric fish *Apteronotus albifrons*. *Journal of Comparative Physiology A-Sensory Neural & Behavioral Physiology* 147:287-297.
- Bastian J (1995) Pyramidal-cell plasticity in weakly electric fish: a mechanism for attenuating responses to reafferent electrosensory inputs. *Journal of Comparative Physiology A-Sensory Neural & Behavioral Physiology* 176:63-73.
- Benda J, Maler L, Longtin A (2010) Linear versus nonlinear signal transmission in neuron models with adaptation currents or dynamic thresholds. *J Neurophysiol* 104:2806-2820.
- Berman N, Maler L (1998a) Inhibition evoked from primary afferents in the electrosensory lateral line lobe of the weakly electric fish (*Apteronotus leptorhynchus*). *Journal of Neurophysiology* 80:3173-3196.
- Berman N, Dunn RJ, Maler L (2001) Function of NMDA receptors and persistent sodium channels in a feedback pathway of the electrosensory system. *Journal of Neurophysiology* 86:1612-1621.
- Berman NJ, Plant J, Turner R, Maler L (1997) Excitatory amino acid transmission at a feedback pathway in the electrosensory system. *Journal of Neurophysiology* 78:1869-1881.
- Carr CE, Maler L, Sas E (1982) Peripheral organization and central projections of the electrosensory organs in gymnotiform fish. *Journal of Comparative Neurology* 211:139-153.
- Ceballos CC, Li S, Roque AC, Tzounopoulos T, Leao RM (2016) Ih Equalizes Membrane Input Resistance in a Heterogeneous Population of Fusiform Neurons in the Dorsal Cochlear Nucleus. *Front Cell Neurosci* 10:249.
- Chacron MJ, Lindner B, Longtin A (2007) Threshold fatigue and information transfer. *J Comput Neurosci* 23:301-311.
- Dangelmayer S, Benda J, Grewe J (2016) Weakly electric fish learn both visual and electrosensory cues in a multisensory object discrimination task. *J Physiol Paris* 110:182-189.
- Deuker L, Bellmund JL, Navarro Schroder T, Doeller CF (2016) An event map of memory space in the hippocampus. *Elife* 5.
- Diamantaki M, Frey M, Berens P, Preston-Ferrer P, Burgalossi A (2016) Sparse activity of identified dentate granule cells during spatial exploration. *Elife* 5.
- Eichenbaum H (2014) Time cells in the hippocampus: a new dimension for mapping memories. *Nat Rev Neurosci* 15:732-744.
- Eichenbaum H (2017) On the Integration of Space, Time, and Memory. *Neuron* 95:1007-1018.
- Ellerkmann RK, Riazanski V, Elger CE, Urban BW, Beck H (2001) Slow recovery from inactivation regulates the availability of voltage-dependent Na(+) channels in hippocampal granule cells, hilar neurons and basket cells. *J Physiol* 532:385-397.
- Elliott SB, Harvey-Girard E, Giassi AC, Maler L (2016) Hippocampal-like circuitry in the pallium of an electric fish: Possible substrates for recursive pattern separation and completion. *The Journal of Comparative Neurology*.

- 855 Elliott SB, Harvey-Girard E, Giassi AC, Maler L (2017) Hippocampal-like circuitry in the
856 pallium of an electric fish: Possible substrates for recursive pattern separation and
857 completion. *J Comp Neurol* 525:8-46.
- 858 Ellis LD, Maler L, Dunn RJ (2008) Differential distribution of SK channel subtypes in the brain
859 of the weakly electric fish *Apteronotus leptorhynchus*. *J Comp Neurol* 507:1964-1978.
- 860 Ellis LD, Mehaffey WH, Harvey-Girard E, Turner RW, Maler L, Dunn RJ (2007) SK channels
861 provide a novel mechanism for the control of frequency tuning in electrosensory neurons.
862 *J Neurosci* 27:9491-9502.
- 863 Favre-Bulle IA, Vanwalleghe G, Taylor MA, Rubinsztein-Dunlop H, Scott EK (2018)
864 Cellular-Resolution Imaging of Vestibular Processing across the Larval Zebrafish Brain.
865 *Curr Biol* 28:3711-3722 e3713.
- 866 Fleidervish IA, Friedman A, Gutnick MJ (1996) Slow inactivation of Na⁺ current and slow
867 cumulative spike adaptation in mouse and guinea-pig neocortical neurones in slices. *J*
868 *Physiol* 493 (Pt 1):83-97.
- 869 Fotowat H, Lee C, Jun JJ, Maler L (2019) Neural activity in a hippocampus-like region of the
870 teleost pallium is associated with active sensing and navigation. *Elife* 8.
- 871 Ganz J, Kroehne V, Freudenreich D, Machate A, Geffarth M, Braasch I, Kaslin J, Brand M
872 (2014) Subdivisions of the adult zebrafish pallium based on molecular marker analysis.
873 *F1000Research* 3:308.
- 874 Gentet LJ, Stuart GJ, Clements JD (2000) Direct measurement of specific membrane capacitance
875 in neurons. *Biophys J* 79:314-320.
- 876 Giassi AC, Ellis W, Maler L (2012a) The Organization of the Gymnotiform Fish Pallium in
877 Relation to Learning and Memory: III. Intrinsic connections. *Journal of Comparative*
878 *Neurology* 520 3369–3394.
- 879 Giassi AC, Maler L, Moreira JE, Hoffmann A (2011) Glomerular nucleus of the weakly electric
880 fish, *Gymnotus* sp.: cytoarchitecture, histochemistry, and fiber connections--insights
881 from neuroanatomy to evolution and behavior. *J Comp Neurol* 519:1658-1676.
- 882 Giassi AC, Duarte TT, Ellis W, Maler L (2012b) The Organization of the Gymnotiform Fish
883 Pallium in Relation to Learning and Memory: II. Extrinsic connections. *Journal of*
884 *Comparative Neurology* 520:3338–3368.
- 885 Giassi AC, Harvey-Girard E, Valsamis B, Maler L (2012c) The Organization of the
886 Gymnotiform Fish Pallium in Relation to Learning and Memory: I. Cytoarchitectonics
887 and Cellular Structure. *Journal of Comparative Neurology* 520:3314–3337.
- 888 Gonzalez JC, Epps SA, Markwardt SJ, Wadiche JI, Overstreet-Wadiche L (2018) Constitutive
889 and Synaptic Activation of GIRK Channels Differentiates Mature and Newborn Dentate
890 Granule Cells. *J Neurosci* 38:6513-6526.
- 891 Graff C, Kaminski G, Gresty M, Ohlmann T (2004) Fish perform spatial pattern recognition and
892 abstraction by exclusive use of active electrolocation. *Curr Biol* 14:818-823.
- 893 Hartley T, Lever C, Burgess N, O'Keefe J (2014) Space in the brain: how the hippocampal
894 formation supports spatial cognition. *Philos Trans R Soc Lond B Biol Sci* 369:20120510.
- 895 Harvey-Girard E, Maler L (2013) Dendritic SK channels convert NMDA-R-dependent LTD to
896 burst timing-dependent plasticity. *J Neurophysiol* 110:2689-2703.
- 897 Harvey-Girard E, Dunn RJ, Maler L (2007) Regulated expression of N-methyl-D-aspartate
898 receptors and associated proteins in teleost electrosensory system and telencephalon. *J*
899 *Comp Neurol* 505:644-668.

- Harvey-Girard E, Giassi AC, Ellis W, Maler L (2012) The Organization of the Gymnotiform Fish Pallium in Relation to Learning and Memory: IV. Expression of Conserved Transcription Factors and Implications for the Evolution of Dorsal Telencephalon. *Journal of Comparative Neurology* 520:3395–3413.
- Harvey-Girard E, Tweedle J, Ironstone J, Cuddy M, Ellis W, Maler L (2010) Long-term recognition memory of individual conspecifics is associated with telencephalic expression of Egr-1 in the electric fish *Apteronotus leptorhynchus*. *J Comp Neurol* 518:2666-2692.
- Henze DA, Buzsaki G (2001) Action potential threshold of hippocampal pyramidal cells in vivo is increased by recent spiking activity. *Neuroscience* 105:121-130.
- Heys JG, Dombeck DA (2018) Evidence for a subcircuit in medial entorhinal cortex representing elapsed time during immobility. *Nat Neurosci* 21:1574-1582.
- Itskov V, Curto C, Pastalkova E, Buzsaki G (2011) Cell assembly sequences arising from spike threshold adaptation keep track of time in the hippocampus. *J Neurosci* 31:2828-2834.
- Itskov V, Pastalkova E, Mizuseki K, Buzsaki G, Harris KD (2008) Theta-mediated dynamics of spatial information in hippocampus. *J Neurosci* 28:5959-5964.
- Jun JJ, Longtin A, Maler L (2016) Active sensing associated with spatial learning reveals memory-based attention in an electric fish. *J Neurophysiol* 115:2577-2592.
- Jung HY, Mickus T, Spruston N (1997) Prolonged sodium channel inactivation contributes to dendritic action potential attenuation in hippocampal pyramidal neurons. *J Neurosci* 17:6639-6646.
- Krahe R, Maler L (2014) Neural maps in the electrosensory system of weakly electric fish. *Curr Opin Neurobiol* 24C:13-21.
- Kraus BJ, Robinson RJ, 2nd, White JA, Eichenbaum H, Hasselmo ME (2013) Hippocampal "Time Cells": Time versus Path Integration. *Neuron* 78:1090-1101.
- Lujan R, Aguado C (2015) Localization and Targeting of GIRK Channels in Mammalian Central Neurons. *Int Rev Neurobiol* 123:161-200.
- Luscher C, Slesinger PA (2010) Emerging roles for G protein-gated inwardly rectifying potassium (GIRK) channels in health and disease. *Nat Rev Neurosci* 11:301-315.
- MacDonald CJ, Lepage KQ, Eden UT, Eichenbaum H (2011) Hippocampal "time cells" bridge the gap in memory for discontinuous events. *Neuron* 71:737-749.
- Maler L (1979) The posterior lateral line lobe of certain gymnotiform fish. Quantitative light microscopy. *Journal of Comparative Neurology* 183:323-363.
- Maler L, Sas EK, Rogers J (1981) The cytology of the posterior lateral line lobe of high frequency weakly electric fish (*Gymnotoidei*): Dendritic differentiation and synaptic specificity in a simple cortex. *Journal of Comparative Neurology* 195:87-139.
- Marcoux CM, Clarke SE, Nesse WH, Longtin A, Maler L (2016) Balanced ionotropic receptor dynamics support signal estimation via voltage-dependent membrane noise. *J Neurophysiol* 115:530-545.
- Martinez D, Metzen MG, Chacron MJ (2016) Electrosensory processing in *Apteronotus albifrons*: implications for general and specific neural coding strategies across wave-type weakly electric fish species. *J Neurophysiol* 116:2909-2921.
- Mathieson WB, Maler L (1988) Morphological and electrophysiological properties of a novel *in vitro* preparation: the electrosensory lateral line lobe brain slice. *Journal of Comparative Physiology A* 163:489-506.

- 945 Mickus T, Jung H, Spruston N (1999) Properties of slow, cumulative sodium channel
946 inactivation in rat hippocampal CA1 pyramidal neurons. *Biophys J* 76:846-860.
- 947 Modi MN, Dhawale AK, Bhalla US (2014) CA1 cell activity sequences emerge after
948 reorganization of network correlation structure during associative learning. *Elife*
949 3:e01982.
- 950 Mueller T, Wullimann MF (2009) An evolutionary interpretation of teleostean forebrain
951 anatomy. *Brain Behav Evol* 74:30-42.
- 952 Newport C, Wallis G, Reshitnyk Y, Siebeck UE (2016) Discrimination of human faces by
953 archerfish (*Toxotes chatareus*). *Sci Rep* 6:27523.
- 954 Northcutt RG (2006) Connections of the lateral and medial divisions of the goldfish
955 telencephalic pallium. *J Comp Neurol* 494:903-943.
- 956 Northcutt RG (2008) Forebrain evolution in bony fishes. *Brain Res Bull* 75:191-205.
- 957 Pastalkova E, Itskov V, Amarasingham A, Buzsaki G (2008) Internally generated cell assembly
958 sequences in the rat hippocampus. *Science* 321:1322-1327.
- 959 Perkins KL, Wong RK (1995) Intracellular QX-314 blocks the hyperpolarization-activated
960 inward current *I_h* in hippocampal CA1 pyramidal cells. *J Neurophysiol* 73:911-915.
- 961 Platkiewicz J, Brette R (2010) A threshold equation for action potential initiation. *PLoS Comput*
962 *Biol* 6:e1000850.
- 963 Platkiewicz J, Brette R (2011) Impact of fast sodium channel inactivation on spike threshold
964 dynamics and synaptic integration. *PLoS Comput Biol* 7:e1001129.
- 965 Rajan K, Harvey CD, Tank DW (2016) Recurrent Network Models of Sequence Generation and
966 Memory. *Neuron* 90:128-142.
- 967 Ranganath C, Hsieh LT (2016) The hippocampus: a special place for time. *Ann N Y Acad Sci*
968 1369:93-110.
- 969 Rischawy I, Schuster S (2013) Visual search in hunting archerfish shares all hallmarks of human
970 performance. *J Exp Biol* 216:3096-3103.
- 971 Rodriguez F, Lopez JC, Vargas JP, Gomez Y, Broglio C, Salas C (2002) Conservation of spatial
972 memory function in the pallial forebrain of reptiles and ray-finned fishes. *J Neurosci*
973 22:2894-2903.
- 974 Rodríguez F, López JC, Vargas JP, Gómez Y, Broglio C, Salas C (2002) Conservation of spatial
975 memory function in the pallial forebrain of reptiles and ray-finned fishes. *J Neurosci*
976 22:2894-2903.
- 977 Salazar BC, Castillo C, Diaz ME, Recio-Pinto E (1996) Multiple open channel states revealed by
978 lidocaine and QX-314 on rat brain voltage-dependent sodium channels. *J Gen Physiol*
979 107:743-754.
- 980 Salisbury JP, Sirbulescu RF, Moran BM, Auclair JR, Zupanc GK, Agar JN (2015) The central
981 nervous system transcriptome of the weakly electric brown ghost knifefish (*Apteronotus*
982 *leptorhynchus*): de novo assembly, annotation, and proteomics validation. *BMC*
983 *Genomics* 16:166.
- 984 Schluessel V, Bleckmann H (2005) Spatial memory and orientation strategies in the
985 elasmobranch *Potamotrygon motoro*. *J Comp Physiol A Neuroethol Sens Neural Behav*
986 *Physiol* 191:695-706.
- 987 Schulze L, Henninger J, Kadobianskyi M, Chaigne T, Faustino AI, Hakiy N, Albadri S, Schuelke
988 M, Maler L, Del Bene F, Judkewitz B (2018) Transparent *Danionella translucida* as a
989 genetically tractable vertebrate brain model. *Nat Methods* 15:977-983.

- 990 Sekerli M, Del Negro CA, Lee RH, Butera RJ (2004) Estimating action potential thresholds from
 991 neuronal time-series: new metrics and evaluation of methodologies. *IEEE Trans Biomed*
 992 *Eng* 51:1665-1672.
- 993 Siebeck UE, Litherland L, Wallis GM (2009) Shape learning and discrimination in reef fish. *J*
 994 *Exp Biol* 212:2113-2119.
- 995 Simms BA, Zamponi GW (2014) Neuronal voltage-gated calcium channels: structure, function,
 996 and dysfunction. *Neuron* 82:24-45.
- 997 Slesinger PA (2001) Ion selectivity filter regulates local anesthetic inhibition of G-protein-gated
 998 inwardly rectifying K⁺ channels. *Biophys J* 80:707-718.
- 999 Talbot MJ, Sayer RJ (1996) Intracellular QX-314 inhibits calcium currents in hippocampal CA1
 1000 pyramidal neurons. *Journal of Neurophysiology* 76:2120-2124.
- 1001 Trinh AT, Harvey-Girard E, Teixeira F, Maler L (2016) Cryptic laminar and columnar
 1002 organization in the dorsolateral pallium of a weakly electric fish. *J Comp Neurol*
 1003 524:408-428.
- 1004 Tsien RW, Lipscombe D, Madison DV, Bley KR, Fox AP (1988) Multiple types of neuronal
 1005 calcium channels and their selective modulation. *Trends Neurosci* 11:431-438.
- 1006 Turner RW, Maler L, Deerinck T, Levinson SR, Ellisman MH (1994) TTX-sensitive dendritic
 1007 sodium channels underlie oscillatory discharge in a vertebrate sensory neuron. *The*
 1008 *Journal of Neuroscience* 14:6453-6471.
- 1009 Vinepinsky E, Perchik S, Ben-Shahar O, Donchin O, Segev R (2018) Representation of Border,
 1010 Velocity and Speed in the Goldfish Brain. *bioRxiv*:291013.
- 1011 Vonderschen K, Chacron MJ (2011) Sparse and dense coding of natural stimuli by distinct
 1012 midbrain neuron subpopulations in weakly electric fish. *Journal of neurophysiology*
 1013 106:3102-3118.
- 1014 Wallach A, Harvey-Girard E, Jun JJ, Longtin A, Maler L (2018) A time-stamp mechanism may
 1015 provide temporal information necessary for egocentric to allocentric spatial
 1016 transformations. *Elife* 7.
- 1017 Wang XJ (1999) Synaptic basis of cortical persistent activity: the importance of NMDA
 1018 receptors to working memory. *J Neurosci* 19:9587-9603.
- 1019 Wimmer K, Nykamp DQ, Constantinidis C, Compte A (2014) Bump attractor dynamics in
 1020 prefrontal cortex explains behavioral precision in spatial working memory. *Nat Neurosci*
 1021 17:431-439.
- 1022 Yamamoto N, Ito H (2008) Visual, lateral line, and auditory ascending pathways to the dorsal
 1023 telencephalic area through the rostromedial region of the lateral preglomerular nucleus in
 1024 cyprinids. *J Comp Neurol* 508:615-647.
- 1025 Yamamoto N, Ishikawa Y, Yoshimoto M, Xue HG, Bahaxar N, Sawai N, Yang CY, Ozawa H,
 1026 Ito H (2007) A new interpretation on the homology of the teleostean telencephalon based
 1027 on homology and a new eversion model. *Brain Behav Evol* 69:96-104.
- 1028 Zhou W, Arrabit C, Choe S, Slesinger PA (2001) Mechanism underlying bupivacaine inhibition
 1029 of G protein-gated inwardly rectifying K⁺ channels. *Proc Natl Acad Sci U S A* 98:6482-
 1030 6487.
- 1031 Zutshi I, Fu ML, Lilascharoen V, Leutgeb JK, Lim BK, Leutgeb S (2018) Recurrent circuits
 1032 within medial entorhinal cortex superficial layers support grid cell firing. *Nat Commun*
 1033 9:3701.

1034

1035 **Figure Legends:**

1036

1037 **Figure 1.** Anatomy of the *Apteronotus leptorhynchus* telencephalon. **A.** A transverse section
1038 through the *Apteronotus* telencephalon indicating the major subdivisions of pallium and
1039 subpallium; this section was obtained from a standard series of cresyl violet stained sections (Elliot
1040 et al, 2017). Midbrain sensory inputs entering the pallium from PG terminates in the dorsolateral
1041 pallium (DL). These inputs are processed within the DL recurrent network (Trinh et al., 2016). DL
1042 projects to the core dorsocentral pallium (DCc) which, in turn, projects to midbrain sensory
1043 regions. DLv is located ventral to DL and distinguished by its olfactory bulb input. The dorsal-
1044 dorsal pallium (DD) has reciprocal connections with DL (Elliott et al., 2017). Scale bar: 500 μ m.
1045 **B.** A higher magnification of the cells in DL illustrates an apparent random distribution and its
1046 highly organized intrinsic laminar and columnar circuitry is not evident (Trinh et al., 2016). The
1047 neurons in DL have homogenous morphology and are roughly 10 μ m in diameter (Giassi et al.,
1048 2012c). Scale bar: 50 μ m. **C.** An infrared image of a DL neuron undergoing a whole-cell patch
1049 recording. The shadow to the left illustrates the patch pipette, while the white arrow highlights the
1050 patched cell. Scale bar: 20 μ m.

1051 Abbreviations: DCc – dorsocentral pallium, core; DCs – dorsocentral pallium, shell; DD – dorsodorsal
1052 pallium; DL – dorsolateral pallium; DLv – dorsolateral pallium, ventral subdivision; DM – dorsomedial
1053 pallium; SP – subpallium.

1054

1055 **Figure 2.** Resting membrane potential of DL neurons. **A.** Three example resting membrane
1056 potential (RMP) traces taken from 3 different ‘quiet’ neurons illustrate the membrane potential at
1057 which these cells would normally stabilize at naturally (*i.e.* no holding current was applied). The
1058 RMP at the start of the recording is shown above each trace. **B.** Three example RMP traces taken
1059 from three different ‘noisy’ neurons in which no holding current was applied. In contrast to the
1060 ‘quiet cells,’ these cells exhibited strong membrane fluctuations even when they had stabilized at
1061 a hyperpolarized potential. **C.** A histogram of the RMP variance for *Apteronotus* (grey) and
1062 goldfish (black) DL neurons showing that most neurons were of the ‘quiet’ type where ‘n’ is the
1063 number of individual 10 s recording traces that were recorded from all cells. (*Apteronotus*, N = 29
1064 cells; goldfish, N = 7 cells; total n = 85 recordings). **D.** A histogram of the natural RMPs in both
1065 the *Apteronotus* and in the goldfish illustrating that the average resting membrane potential of DL
1066 neurons is around -77 mV in *Apteronotus* and around -73 mV in goldfish (*Apteronotus*, N = 35
1067 cells; goldfish, N = 11 cells; total n = 71 recordings). **E.** A noisy DL neuron’s response to the
1068 injection of ± 37.5 pA current steps in *Apteronotus*, illustrating that the membrane fluctuations are
1069 invariant to the membrane potential of the cell. **F.** A scatter plot of the variance and membrane
1070 potential, including all recordings (black dots) that had a variance value above 0.5 mV^2
1071 (*Apteronotus*, N = 6 cells; goldfish; N = 4 cells; total n = 20 recordings).
1072

1073 **Figure 3.** Noisy cells. **A.** Example recording trace from a noisy cell displaying spontaneous
1074 membrane potential fluctuations. These fluctuations often vary in size but are usually in the range
1075 of several millivolts and can trigger action potentials (spikes), as highlighted by the box showing
1076 a magnified version of the first fluctuation. The arrow within the magnified box highlights an
1077 example of the small fluctuations that precede spiking. **B.** Example trace illustrating a spontaneous
1078 membrane fluctuation that lasted 865.5 ms and produced a short burst of 2 action potentials. **C.** A
1079 higher magnification of the rise phase of the spontaneous fluctuation shown in panel 3B. The
1080 arrows denote small membrane potential fluctuations that appear to summate, giving rise to a
1081 sustained depolarization and spiking. **D.** The top trace illustrates an example recording of a noisy
1082 cell before the addition of a synaptic blocker. The bottom trace illustrates a recording of the same
1083 cell after the addition of 10 mM kynurenic acid. **E.** The average variance of the resting membrane
1084 potential before and after the bath application of 10 mM kynurenic acid (Apteronotus; N = 3 cells,
1085 goldfish; N = 2 cells). Each black square represents a cell from either fish and the grey square
1086 represents the mean variance. The red triangles depicts the average variance of the cell shown in
1087 Fig. 3D. Of particular note, the wide range of variances all decreased to a similar value after the
1088 application of the synaptic blocker. **F.** Same as in E. except this graph depicts the resting membrane
1089 potential (RMP) instead (Apteronotus; N = 3 cells, goldfish; N = 2 cells). Unlike the variance, the
1090 RMP was unaffected by the bath application of the synaptic blocker.

1091

1092 **Figure 4.** Spiking characteristics of DL neurons. **A. (i)** Example of an *Apteronotus* DL quiet
 1093 neuron response to the injection of ± 500 ms current-steps with varying amplitudes as shown below
 1094 the response traces. The latency to the first evoked spike clearly decreases with increasing current
 1095 intensities. However, even at elevated current injections ($+70$ pA), these cells cannot be driven to
 1096 a high firing rate (maximum in this case was 22 Hz). This appears to be due, at least in part, to the
 1097 prominent AHPs that follow the spikes (arrow). There is a large difference between the membrane
 1098 potential responses to depolarizing versus hyperpolarizing current steps – much stronger responses
 1099 are seen to positive current pulses. **(ii)** We illustrate this asymmetry by superimposing the absolute
 1100 responses to equal intensity injections of a hyperpolarizing and subthreshold depolarizing current
 1101 steps; the response to the hyperpolarizing step is inverted for a clear comparison. DL neuron
 1102 recordings in goldfish also yielded a similar asymmetry and spiking patterns (data not shown, but
 1103 see panel 4B). **B.** Example of a goldfish dorsal DL (DLd) neuron response to a standard 500 ms
 1104 current step injection; the region chosen for these recordings receive inputs from PG similar to the
 1105 DL neurons in *Apteronotus*. The responses of these cells were very similar to those of *Apteronotus*
 1106 DL neurons. **C.** Example recording of a DL neuron in response to a single current step injection.
 1107 The arrow highlights the location of the threshold for these neurons (see Panel E). **D. (i)** A single
 1108 spike is evoked for currents near spike threshold. **(ii)** After current injections that induce
 1109 depolarizations exceeding the spike threshold, DL neurons emit a short doublet or triplet burst of
 1110 spikes at a shorter latency (arrow, *Apteronotus* recording; similar behaviour was seen in goldfish
 1111 DL neurons). Note that spike amplitude drops slightly but progressively in the 4C and 4D traces.
 1112 **E.** Histogram of the average threshold of the first current-evoked spike in DL neurons. The spike
 1113 threshold, which was found using the first derivative of the membrane potential, was ~ -45 mV in

1114 *Apteronotus* and ~ -42 mV in goldfish. The total number of spikes across all cells used for these
1115 estimates was $n = 380$ in *Apteronotus* and $n = 154$ in goldfish.
1116

Figure 5. Pharmacological block of sodium and other channels in DL neurons. **A. (i)** This panel illustrates a goldfish DL neuron's membrane potential response to 500 ms current step injections. For +60 pA, large spikes are evoked at a -38.4 mV threshold; in this example, the first spike has a height of 47.5 mV from the threshold and has a half-width of 3.1 ms. **(ii)** The bottom panel shows the responses after bath application of 20 μ M TTX, which completely eliminates the large fast spikes. Delayed, broad spikes (amplitude: 22.7 mV from the threshold, half width: 10.5 ms) are now evoked at elevated current levels (+80 pA) with a spike threshold of -21.0 mV. The arrow indicates the approximate location of the threshold for the broad TTX insensitive spike. **B. (i)** The response of a DL neuron to a current step at the subthreshold membrane potential before (black) and after (grey) application of TTX. After TTX treatment, the membrane potential did not dramatically change compared to control and in some cases **(ii)** the subthreshold membrane potential was even more depolarized than in the control condition. **C. (i)** Response of an *Apteronotus* DL neuron to current injection steps following QX-314 application via the recording pipette. Fast Na^+ spikes are eliminated by this treatment, even with strong current injections (+70 pA, 500 ms) that would always evoke spiking in control neurons. **(ii)** Stronger current injection (+85 pA, 1000 ms), evoked delayed broad spikes (amplitude from the threshold = 36.9 mV, half-width; 25.9 ms) with a higher threshold (-8.3 mV) compared to the TTX-insensitive spikes illustrated in panel **A (i)**. Stronger current injections (+85 pA, 1000 ms) evoked several putative Ca^{2+} spikes with a shorter latency to the first spike. The arrow highlights the approximate location of the threshold of the broad Ca^{2+} spike. **D.** Average I-V relationship obtained from subthreshold *Apteronotus* and goldfish DL recordings without the application of any pharmacological blockers (black squares), after the application of 20 μ M TTX (white triangles), and with the inclusion of QX-314 within the patch pipette solution (white circles). Both the curves for control and TTX are

1140 piecewise linear with the slope being markedly smaller for hyperpolarizing (control; 0.28 ± 0.02
1141 mV/pA, TTX; 0.32 ± 0.04 mV/pA) compared to depolarizing steps (control; 0.69 ± 0.03 mV/pA,
1142 TTX; 0.74 ± 0.03 mV/pA). In contrast, the addition of QX-314 has linearized the I-V curve
1143 (hyperpolarizing slope = 0.60 ± 0.11 mV/pA, depolarizing slope = 0.86 ± 0.12 mV/pA) with its
1144 main effect on the response to hyperpolarizing current injections (see Table 1). Extended
1145 information illustrating the expression of GIRK channels in the *Apteronotid* fish's brain is
1146 available in Extended Data Figure 5-2.

1147

1148 **Figure 6.** SK-mediated potassium channels contribute to the AHP of DL neurons. **A.** *Apteronotus*
1149 DL neuron response to 500 ms step current injection before (black trace) and after the bath
1150 application of 30 μ M UCL1684 (grey trace). The black arrow shows the minimum membrane
1151 potential between two spikes and is used to estimate the amplitude of the AHP by comparison with
1152 the membrane potential immediately preceding the first action potential. The prominent AHPs
1153 seen in the control condition are reduced by this treatment and the spike rate has also increased
1154 (from 3 spikes to 8 spikes). **B.** DL neuron response to the injection of 750 ms current steps before
1155 (black trace) and after bath application of 1 mM EBIO in the goldfish (grey trace; a longer pulse
1156 was needed in order to increase the likelihood of evoking more than one spike). The amplitude of
1157 the AHP (arrow) was increased by this treatment and the spike rate has been reduced (from 4 to 2
1158 Hz). **C.** Average amplitude (**i**) and average area under the membrane potential (**ii**) of the AHP
1159 following the first spike of DL neurons in response to current steps (control, N = 12 cells;
1160 UCL1684, N = 7 cells; EBIO, N = 5 cells). Both the amplitude and the area under the AHP are
1161 significantly diminished after the application of UCL1684, while a strong increase was observed
1162 after the application of EBIO. **D.** Average firing rate plotted as a function of the amount of current
1163 injected for the control condition (black trace), the UCL1684 condition (grey trace) and the EBIO
1164 condition (light grey trace) in both *Apteronotus* and goldfish (control, N = 28 cells; UCL1684, N
1165 = 7 cells; EBIO, N = 5 cells). The firing rate increases for all current injections after UCL1684
1166 application, while the firing rate decreases after the EBIO application.

1167

1168 **Figure 7.** The effect of intracellular Ca^{2+} chelation on DL neuron responses to depolarization. **A.**
1169 Example recording trace (*Apterionotus*) with 10 mM BAPTA added to the internal solution of the
1170 patch pipette. The AHP appears to be completely eliminated which promotes higher frequency
1171 spiking; note that successive spike heights drop continuously for the first seven spikes. By the 8th
1172 spike, very prominent spike broadening begins and the spike height drops to an even greater degree
1173 compared to the UCL1684 application in Fig. 6B. **B.** The average firing rate was plotted as a
1174 function of the amount of current injected for the control (black trace, N = 28 cells), UCL1684
1175 (grey trace, N = 7 cells) and BAPTA conditions (light grey trace, N = 7 cells). The addition of
1176 intracellular BAPTA promotes an even stronger increase in firing rate compared to the addition of
1177 the SK channel blocker UCL1684. **C.** The average difference in spike height between the nth spike
1178 and the first spike was plotted as function of successive spikes obtained after a 500 ms current step
1179 injection for all 3 conditions mentioned in 7B. The addition of UCL1684 did not strongly affect
1180 the spike height, unlike the addition of BAPTA, which reduced the spike height across successive
1181 spikes following a step current injection. The arrow highlights the 8th spike, which marks the
1182 beginning of the non-linearity in the BAPTA condition. **D.** The average spike width was plotted
1183 as a function of successive spikes, similar to panel 7C. UCL1684 application has only a minimal
1184 effect on spike width. The presence of intracellular BAPTA increased the spike width across
1185 successive spikes during a step current injection when compared to the other conditions. The arrow
1186 indicating the 8th spike marks a strong change in spike width, as denoted by the arrow in 7A.
1187

Figure 8. DL neuron spiking causes a decrease in AHP amplitude and an increase in spike threshold. **A.** A magnified view of the first 3 spikes in an example trace of a DL neuron's response to a +60pA current injection where the black dashed line is placed to coincide with the minimum of the first spike's AHP and the grey dashed line is placed to coincide with the first spike's threshold. The black arrows highlight the progressive increase in spike threshold following consecutive spikes. **B.** The increase in spike threshold between the second and first spikes was plotted in the same manner as a function of the first interspike interval (ISI). Individual black squares represent a pair of spikes that were taken from a trace which did not contain an initial burst (total of 160 non-burst pairs), while individual triangles represent a pair of spikes that were taken from a trace displaying an initial burst of spikes as in Fig. 4C (total of 117 burst spike pairs). The majority of the spike thresholds increased (over 300 ms) with no evident recovery. **C.** The difference in average spike threshold between the n^{th} spike and the first spike is plotted as a function of the spike number. The subsequent curve was fit with a double exponential equation ($y = 2.72 * e^{0.04x} - 9.0e^{-0.72x}$; $R^2 = 0.987$). **D.** The increase in spike threshold between the n^{th} spike and the first spike is plotted as a function of the time interval between them. Each black square represents a spike pair (total of 573 spike pairs). Overall, the increase in threshold appears to be larger following longer timer intervals. Extended information related to the modulation of the AHP after prolonged spiking is available in Extended Data Figure 8-2.

Figure 9. DL neuron spike threshold adaptation can last up to hundreds of milliseconds. **A. (i)** Two ramp current injections separated at various times t (50 ms, 500 ms and 1000 ms) were used to measure the time constant of the spike threshold adaptation. Although both ramp current injections have the same slope (slope = 1.3 pA/ms), the objective of the first ramp current was to induce an accumulation of Na^+ channel inactivation through the firing of multiple action potentials and therefore was stronger than the second ramp current which would only produce one action potential. **(ii)** A magnified view of the example responses obtained after the first ramp current injection and after the second ramp current injections at times $t = 50$ ms, 500 ms and 1000 ms respectively. The black dash line is aligned to the first spike's threshold obtained after the first ramp current injection while the grey dotted lines are aligned to the spike threshold obtained from the second ramp current injection for the various times t mentioned previously. **B.** The average difference in spike threshold (for the first spike only) between the first and second ramp current injections were plotted as a function of the time t between each ramp injection. The resulting curve was fitted with an exponential equation ($y = 2.38 * e^{-0.0017x}$, $R^2 = 0.917$). **C.** We used a simplified exponential integrate and fire model with fast ($\tau_f = 15$ ms) and slow ($\tau_s = 500$ ms) Na^+ channel inactivation in an attempt to connect the apparent Na^+ channel inactivation (Fig. 7A) with the increase in spike threshold over multiple spikes (C, D). **(i)** When driven by a step current, the model produces a small number of spikes at frequencies consistent with the data; however, the neuron quickly ceases discharge despite continuous application of the strong positive current. **(ii)** This result can be easily understood in terms of the dynamic spike threshold (θ), which increases because of cumulative slow inactivation of the Na^+ channel (h_f and h_s not shown). Note that the threshold changes by approximately 4 mV (grey shading) over the course of a few spikes, in line with the upper bound for threshold increases seen between DL cell spikes (panel i).

1230 **Extended Data Figure Legends:**

1231

1232 **Figure 5-2.** GIRK channel mRNA expression obtained from RT-PCR in the *Apteronotus* brain
1233 using pan-PCR primer pairs in conserved regions. GIRK channels are ubiquitously expressed
1234 albeit at variable levels. In particular they are expressed in DL.

1235 Abbreviations: SP – subpallium; DL – dorsolateral pallium; TT – Tectum/Torus; Cer – cerebellum;
1236 ELL – electrosensory lobe; HB – hindbrain; ch – chicken (negative control); M – molecular
1237 marker.

1238

1239 **Figure 8-2.** Current-evoked spiking decreases the AHP amplitude of DL neuron. **A.** Example trace
1240 of a DL neuron's response to a +60 pA current step injection lasting 500 ms. Consecutive spiking
1241 causes the AHP amplitude to decrease when compared to the first AHP as emphasized by the
1242 arrow. A black dashed line is placed to coincide with the minimum of the first spike's AHP. We
1243 hypothesize that the decrease in AHP amplitude is due to a reduction in Ca^{2+} influx (*i.e.*, Ca^{2+} -
1244 dependent Ca^{2+} channel inactivation) and subsequent reduction in SK channel opening. **B.** The
1245 decrease in AHP amplitude between the second and first spikes is plotted as a function of the time
1246 interval between the first two spikes similarly to Fig. 8B. Each black square represents a spike pair
1247 taken from a trace which did not contain a burst (total of 160 non-burst spike pairs), while each
1248 grey triangle represents a spike pair taken from a trace which contained a burst at the beginning of
1249 the trace (total of 117 burst spike pairs). The majority of the AHPs are reduced throughout the 300
1250 ms test period without any evident recovery trend.
1251

1252 **Extended Data 1.** Matlab Code for iEIF model.

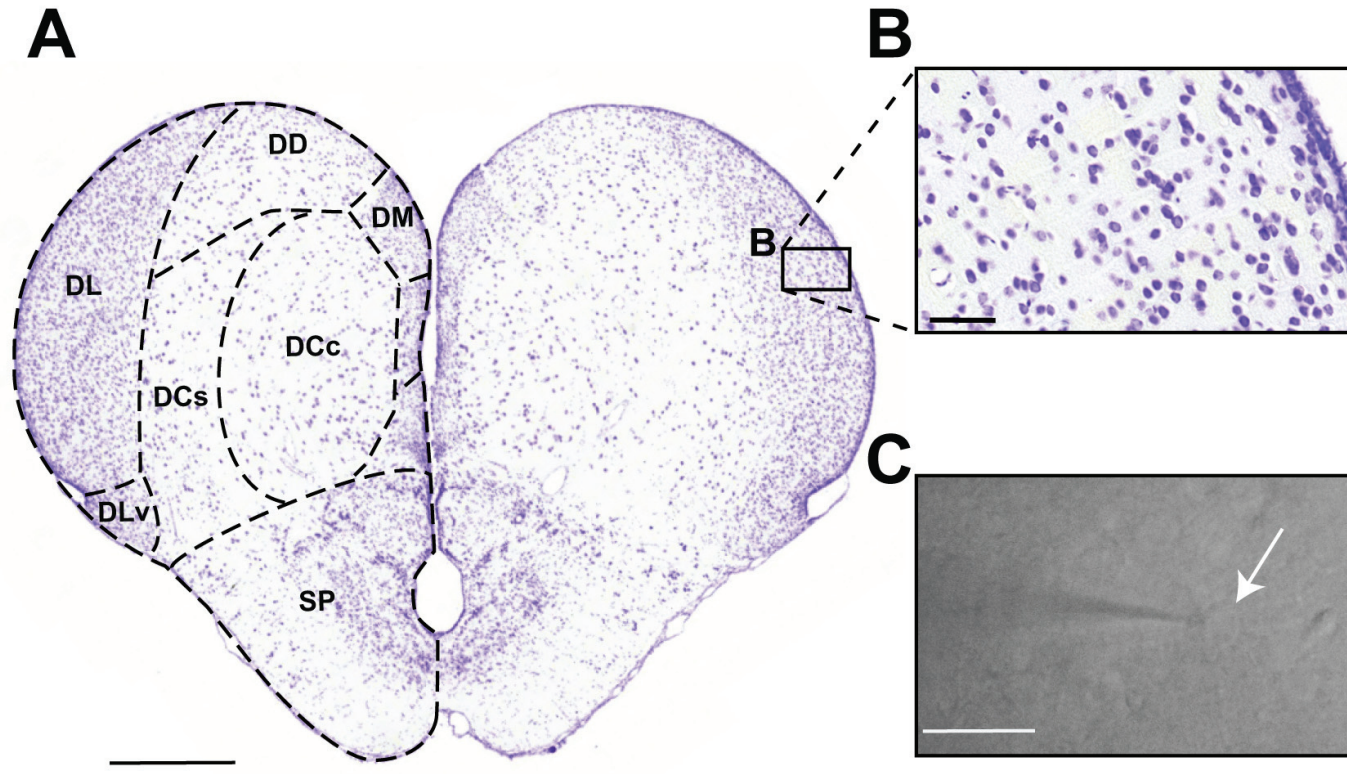
1253 iEIF.zip contains the following files:

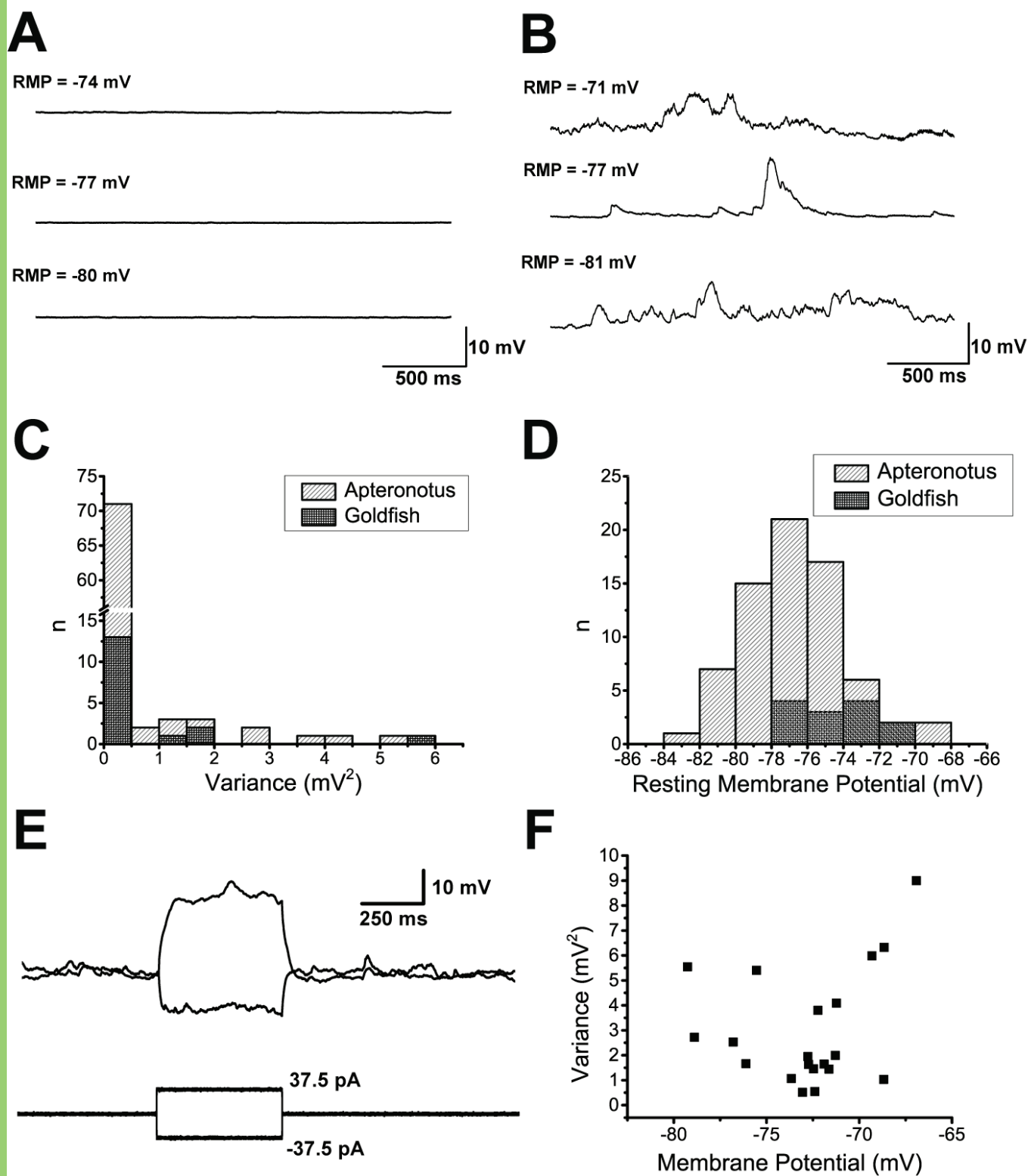
1254 iEIF.m is the main model file.

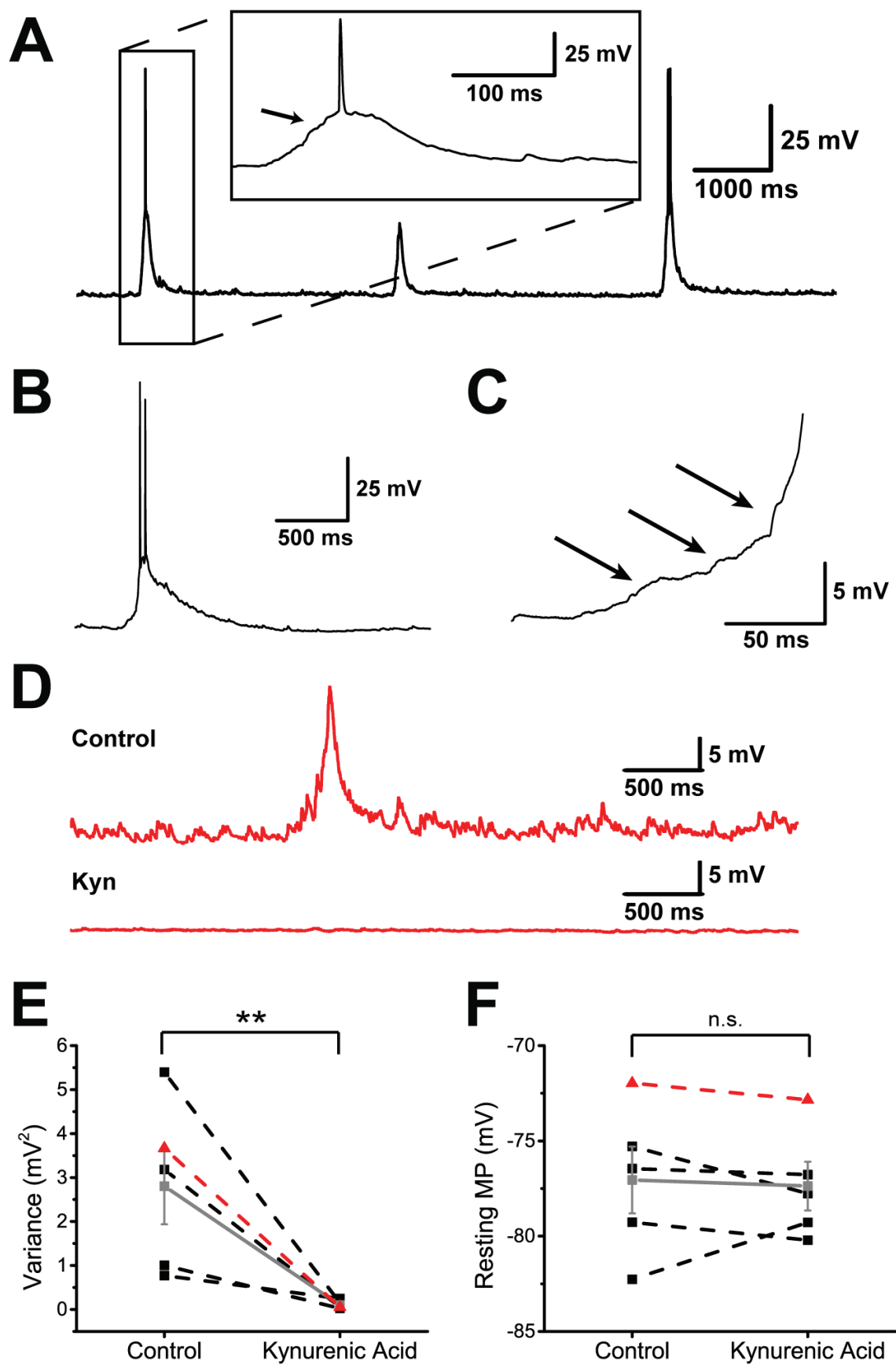
1255 h_inf.m is the Boltzman equation file (this equation is also present in iEIF.m).

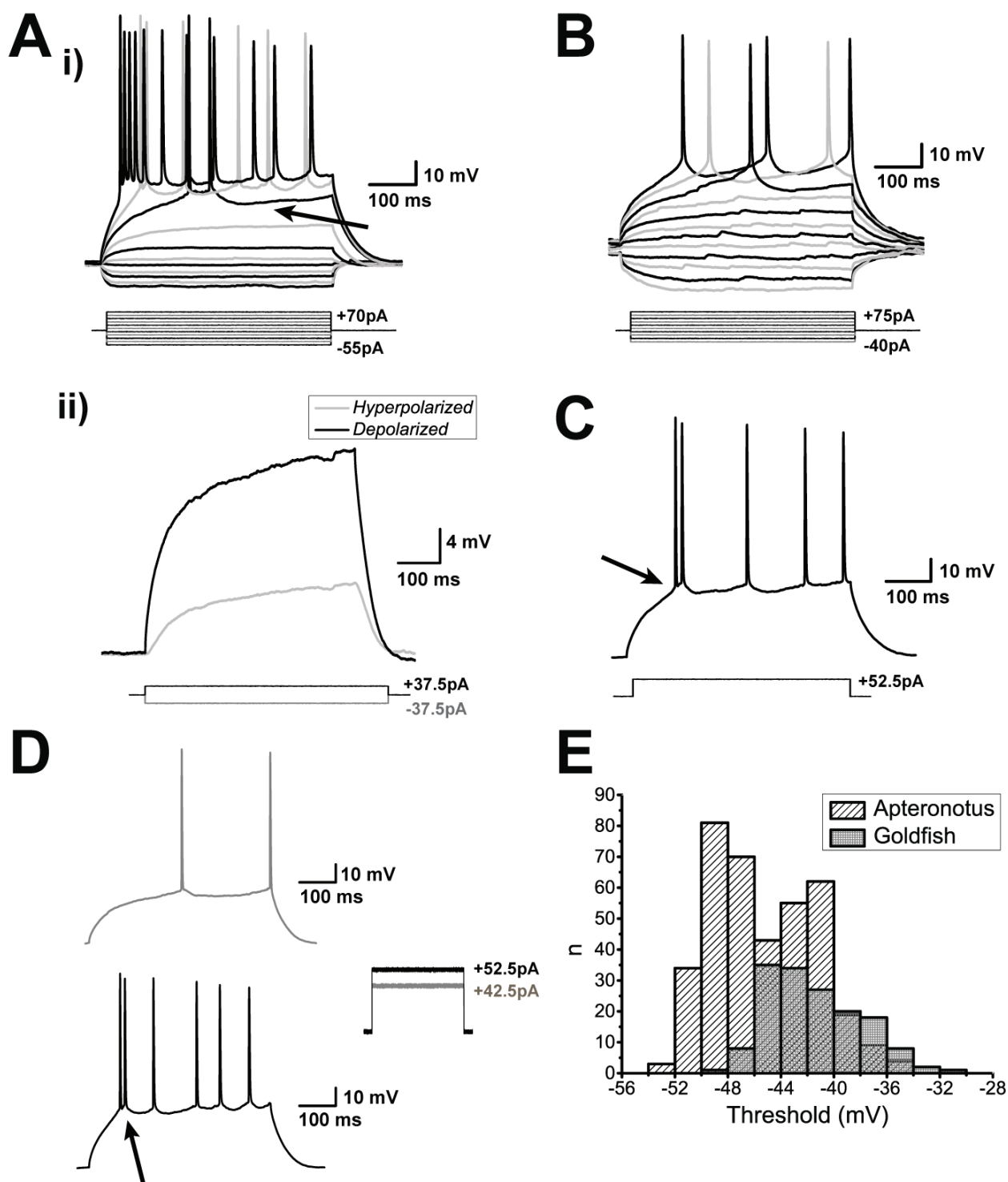
1256 vline.m is a function file used to draw lines on the subplot figures.

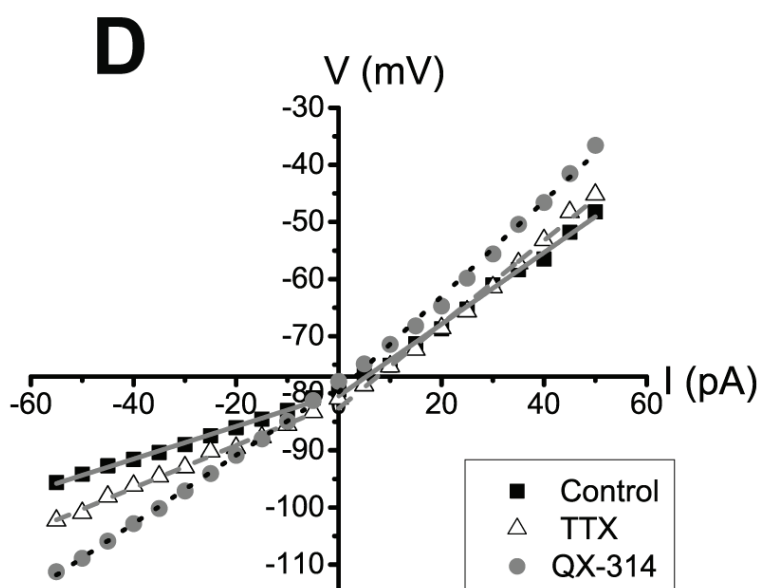
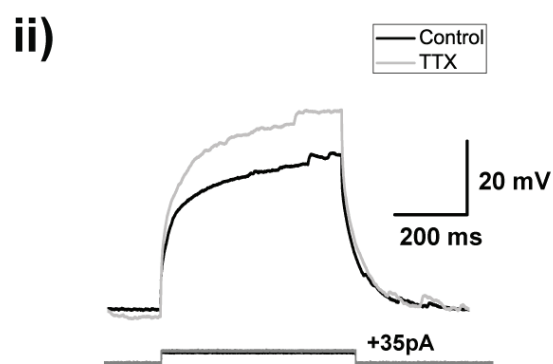
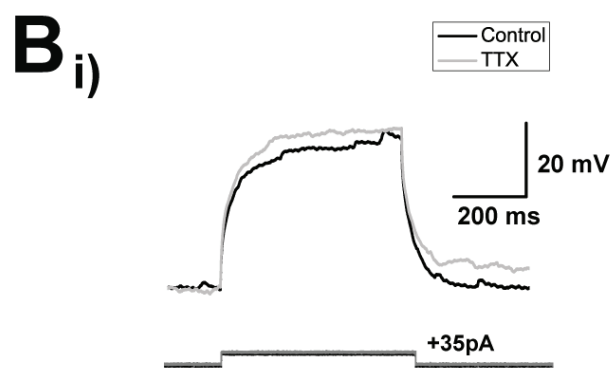
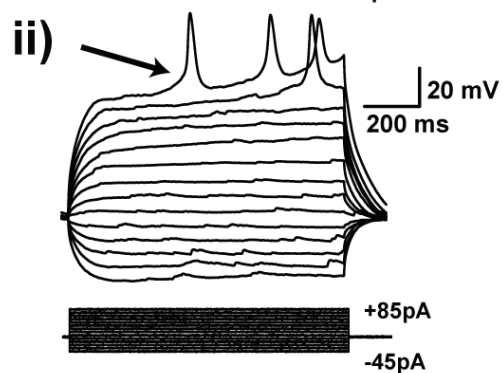
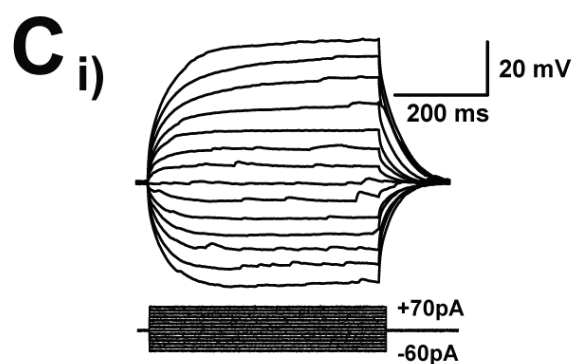
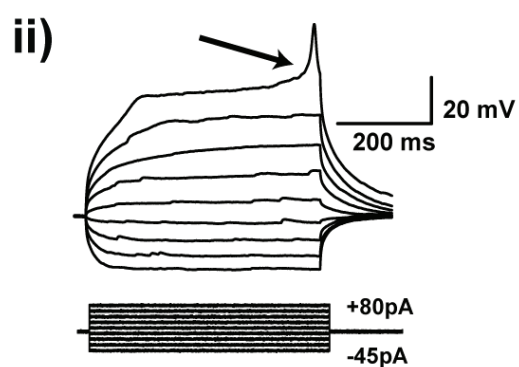
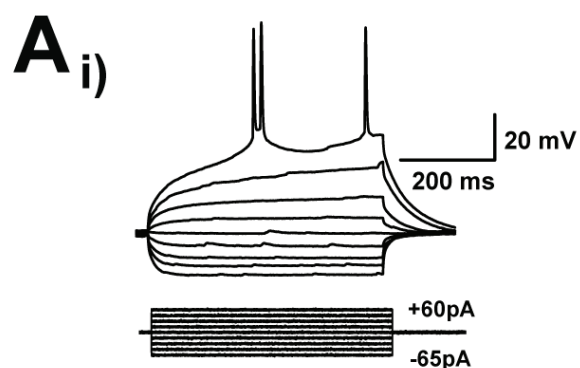
1257

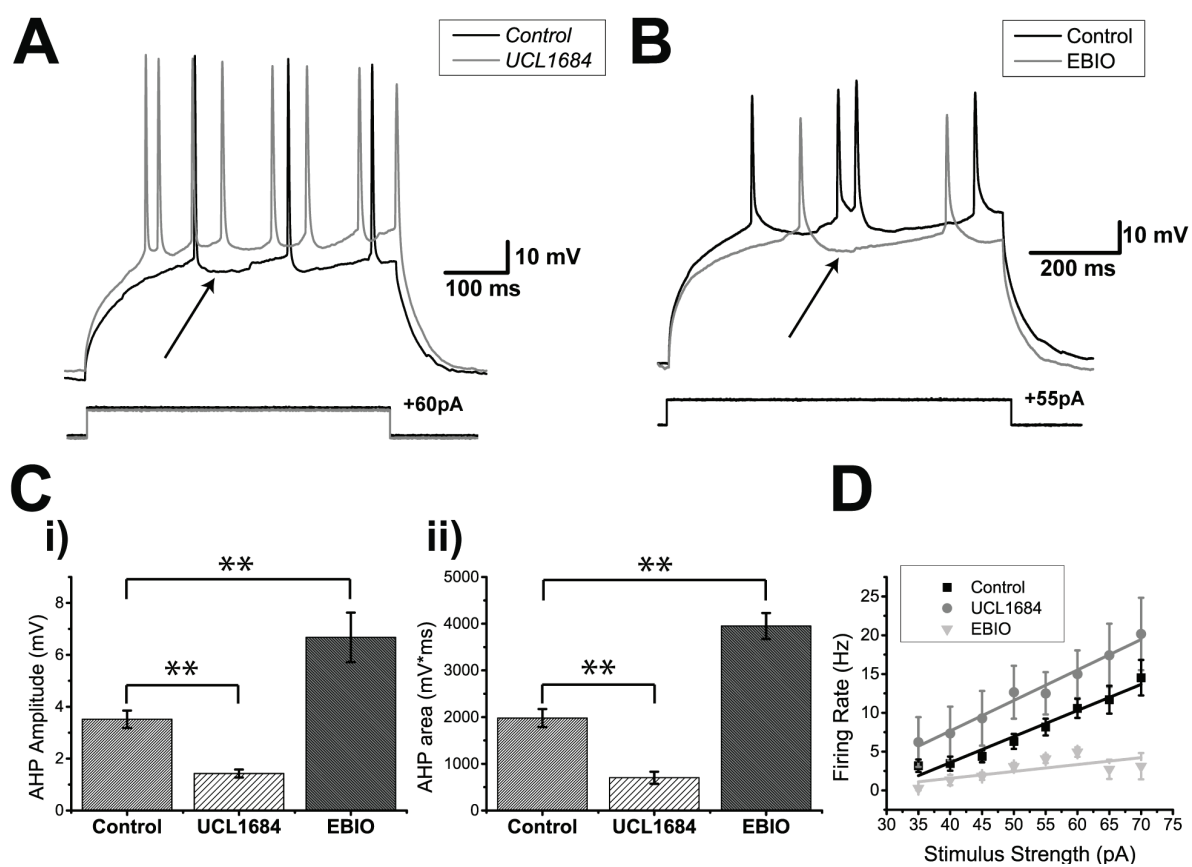


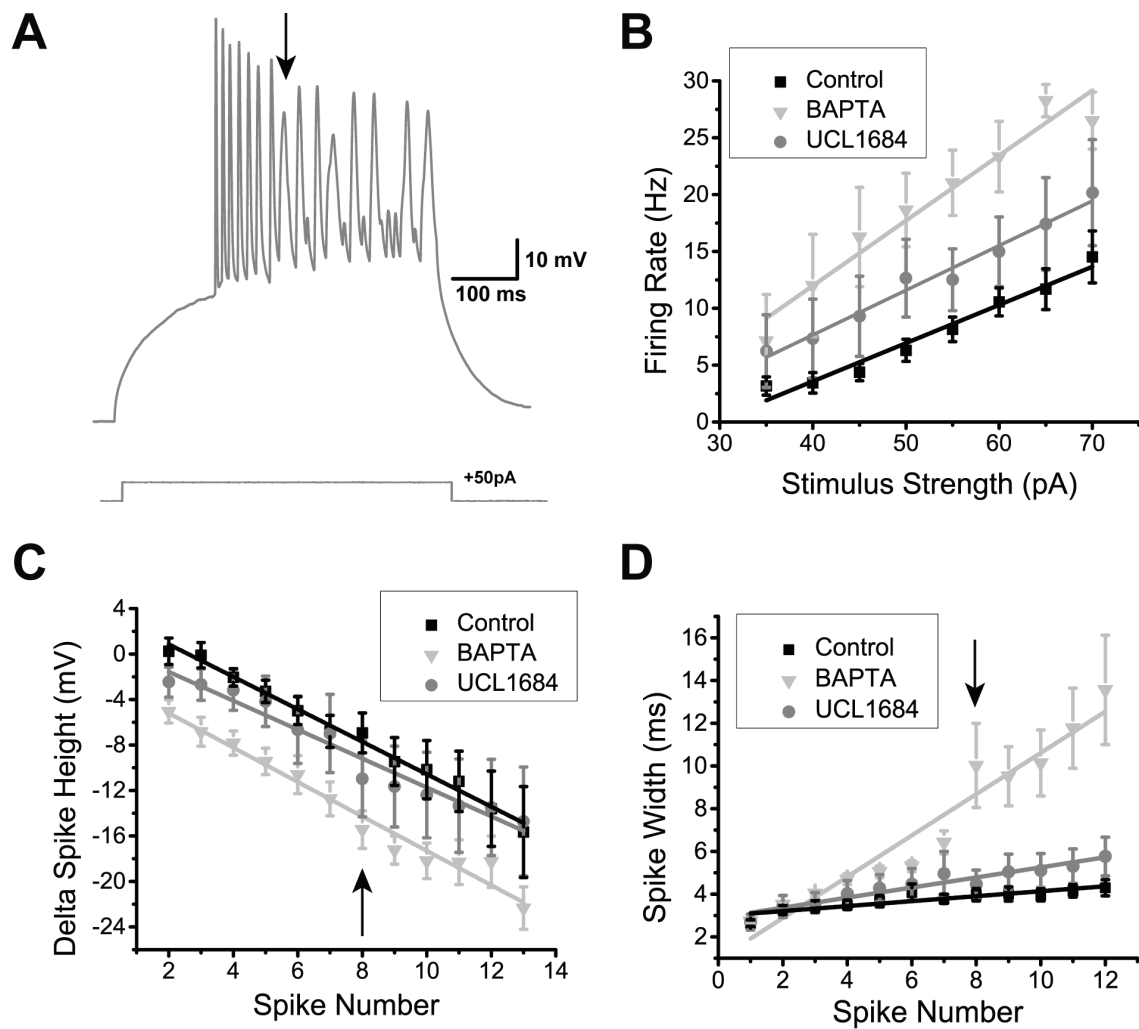


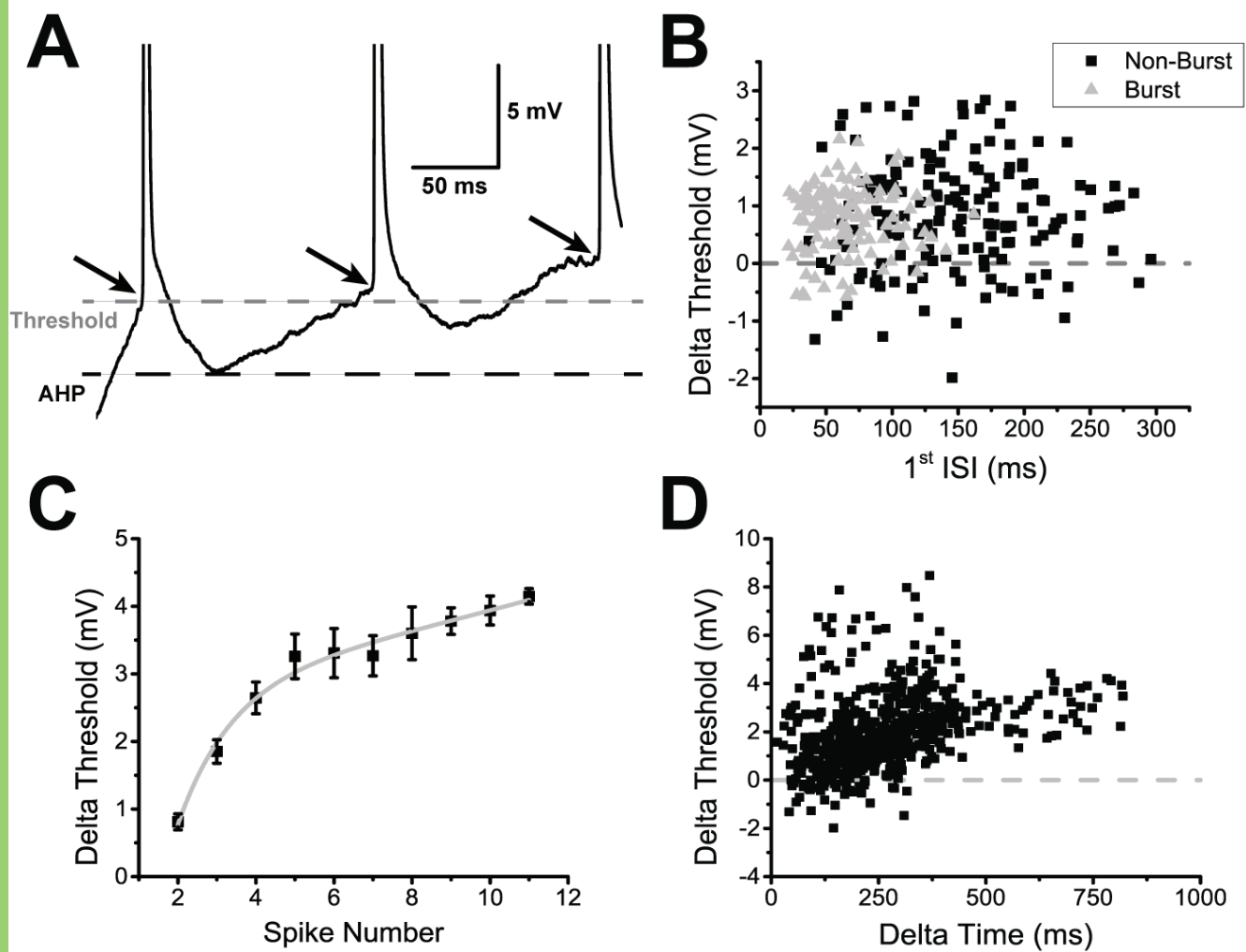












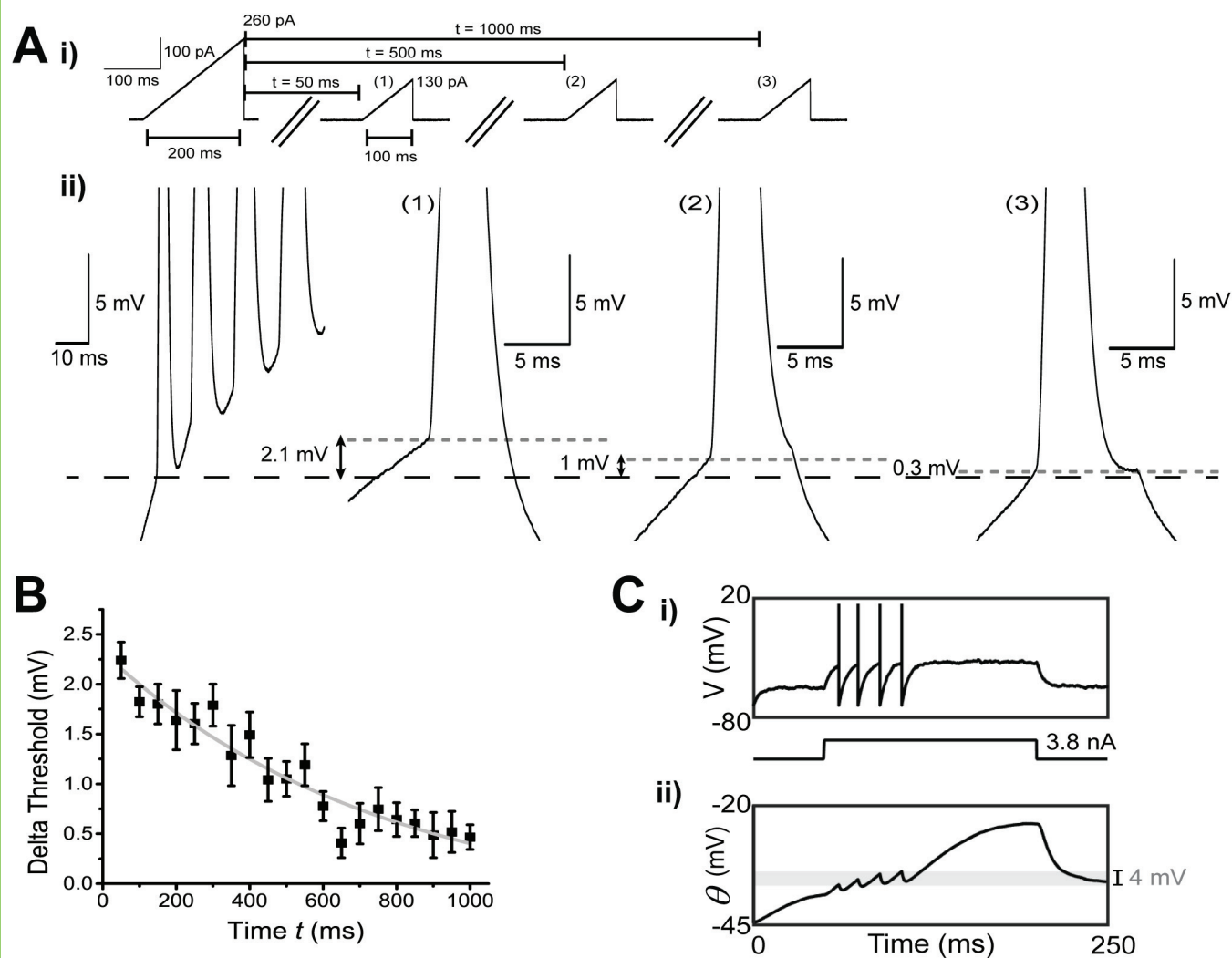


Table 1: I-V slope measurements obtained from the depolarizing and hyperpolarizing responses of DL neurons in both teleost species for both the TTX and QX-314 experiments.

Conditions	Depolarizing Slope (GΩ)	Hyperpolarizing Slope (GΩ)
Control (N = 18 cells)	0.69 ± 0.03	0.28 ± 0.02
TTX (N = 6 cells)	0.74 ± 0.03	0.32 ± 0.04
QX-314 (N = 6 cells)	0.86 ± 0.12	0.60 ± 0.11

Table 2: Difference in spike threshold and resting membrane multiple cell types.

	‘hippocampus’		L4 Sensory cortex		Primary Sens. cells	
Values in mV	DL cells	DG granule cells ^a	Barrel Field ^b	Visual Cortex ^c	ELL Pyr ON cells	DCN Pyr Cells ^f
Spike threshold	-44.2	-40.8	-45.1	~-63.5	-62.9 ^d	-48.1
RMP	-76.2	-74.7	-63.0	-72.0	-67.8 ^e	-62.7
Threshold – RMP	32.0	33.9	17.9	8.5	4.9	14.6

^a Kowalski et al. (2016), *in vivo*, threshold: used point of 1st derivative which exceeded 20 V*s⁻¹.

^b Yu et al. (2016), *in vivo*, threshold: used point of 1st derivative which exceeded 3 times the average 1st derivative.

^c Wilent and Contreras (2005), *in vivo*, threshold: used peak of 2nd derivative, values were averaged from the data for preferred direction and non-preferred direction

^d Mehaffey et al. (2008), *in vitro*, threshold: used point of 1st derivative which was 8 times greater than SD.

^e Berman and Maler (1998a), *in vitro*.

^f Li et al. (2013), *in vitro*, threshold: used point of 1st derivative which exceeded 10 V*s⁻¹.

Table 3: Statistical Table.

Data Structure		Type of Statistical Test	Power
Difference between the average variances of the resting membrane potential	Control vs Kynurenic Acid	Paired-t test	p = 0.0383
Difference between the average resting membrane potential	Control vs Kynurenic Acid	Paired-t test	p = 0.7372
Difference between the input resistance (hyperpolarizing vs depolarizing)	Control	Paired-t test	p = 3.3×10^{-12}
	TTX	Paired-t test	p = 9.9×10^{-6}
	QX-314	Paired-t test	p = 2.3×10^{-4}
Difference between the input resistance for hyperpolarizing current injections	Control vs TTX	One-way ANOVA	n.s. (p = 0.32)
	Control vs QX-314	One-way ANOVA	p = 5.9×10^{-5}
Difference between the input resistance for depolarizing current injections	Control vs TTX	One-way ANOVA	n.s. (p = 0.42)
	Control vs QX-314	One-way ANOVA	p = 0.07
Difference in AHP amplitude	Control vs UCL1684	Two sample t-test	p = 0.0003
	Control vs EBIO	Two sample t-test	p = 0.001
Difference in AHP area under the curve	Control vs UCL1684	Two sample t-test	p = 0.0002
	Control vs EBIO	Two sample t-test	p = 0.00002
Difference in DL neuron current-evoked spiking rate	Control vs UCL1684	Two-way ANOVA	p = 0.0013
	Control vs EBIO	Two-way ANOVA	p = 0.000092

	Control vs BAPTA	Two-way ANOVA	$p = 1.5 \times 10^{-15}$
	UCL1684 vs BAPTA	Two-way ANOVA	$p = 0.00063$
Difference in DL neuron current-evoked spike height	Control vs BAPTA	Two-way ANOVA	$p = 2.1 \times 10^{-12}$
	UCL1684 vs BAPTA	Two-way ANOVA	1.6×10^{-6}
	Control vs UCL1684	Two-way ANOVA	n.s. ($p = 0.14$)
Difference in DL neuron current-evoked spike width	Control vs BAPTA	Two-way ANOVA	$p = 1.3 \times 10^{-31}$
	UCL1684 vs BAPTA	Two-way ANOVA	$p = 3.7 \times 10^{-10}$
	Control vs UCL1684 (first 3 spikes only)	Two-way ANOVA	n.s. ($p = 0.24$)
AHP reduction between 1 st and 2 nd spike	Non-burst spike pairs	One sample t-test	$p = 4.45 \times 10^{-27}$
	Initial burst spike pairs	One sample t-test	$p = 1.26 \times 10^{-13}$
Spike threshold increase between 1 st and 2 nd spike	Non-burst spike pair	One sample t-test	$p = 1.24 \times 10^{-22}$
	Initial burst spike pairs	One sample t-test	$p = 8.30 \times 10^{-28}$